10. MATHEMATICAL MODELING OF OIL SHALE PYROLYSIS

The process of transforming solid kerogen to liquid and gaseous products is complex. Several interrelated physical and chemical phenomena occur simultaneously. Products are formed and exit the mineral matrix at definitive velocities through permeable paths. A pore network is created and the pressure changes during the gaseous product formation due to decomposition of the organic matter. A model created with COMSOL multiphysics for oil shale thermal retorting has been developed. The general kinetic model was integrated with some of the important physical processes which occur during pyrolysis. The effect of the process conditions was also investigated.

10.1. Modeling Framework

The main components of the oil shale pyrolysis process, in a logical sequence are depicted in Figure 10-1. A mathematical representation of the physical phenomena during oil shale pyrolysis is modeled in COMSOL multiphysics simulation suite. COSMOL multiphyics uses finite element method to solve the coupled equations simultaneously. The data visualization is relatively simple. It has the capability to include problem specific equation with existing simulation modules. The purpose of developing this model was to understand the coupling of various phenomena in oil shale pyrolysis and to estimate the effect of operational parameters on product distribution. The model developed in this study includes heat transfer due to conduction and mass transformation due to reaction kinetics. Further, porosity and permeability models were included in the

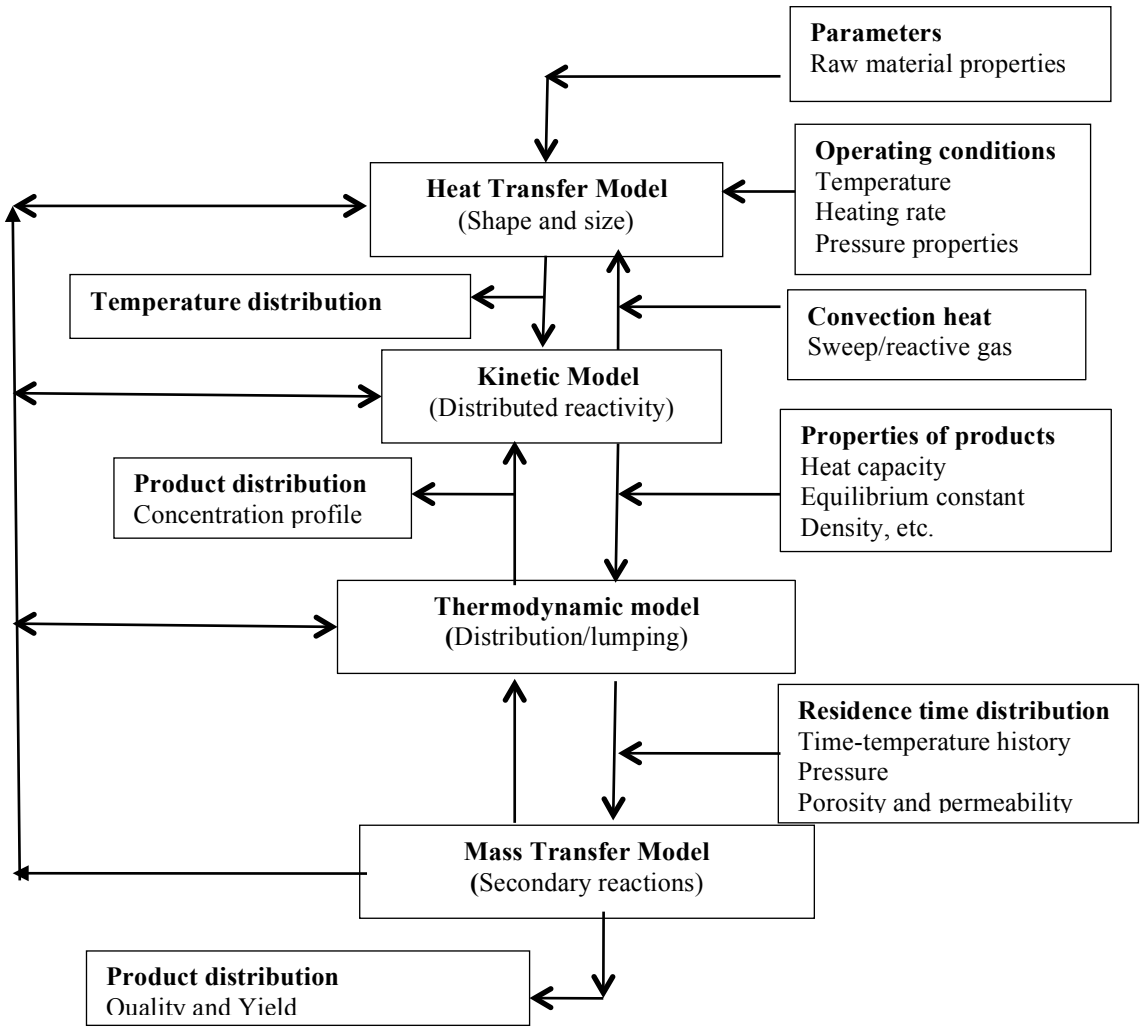

Figure 10- 1: Schematic of the model design to simulate the coupled multiphysics involved in the thermal treatment of oil shale.

framework and convective phenomena in heat and mass balance equations were included. In a shrinking core model, the particle size changes. Hence a grain model concept was applied. It was assumed that the physics vary only in the radial direction. Figure 10-2 shows the geometric representation of simplified simulation scheme adopted in this study. The coupled governing equations were solved simultaneously. Appropriate changes in the physical properties of the material were taken into account as the decomposition process evolved. For example, the propagation of heat conduction within

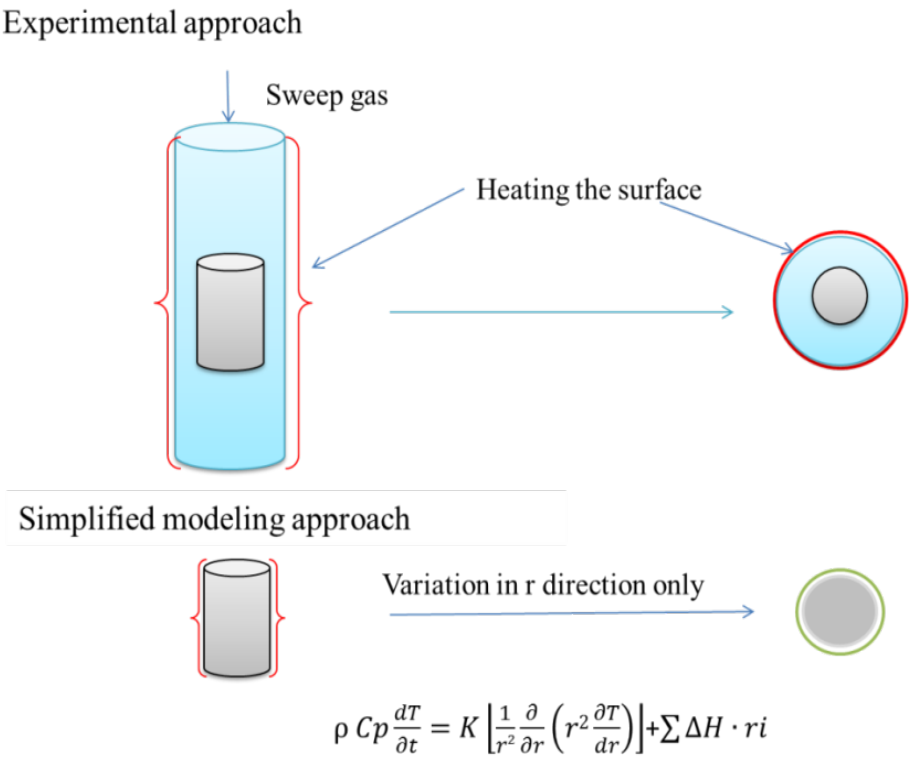

Figure 10- 2: Schematic of experimental approach and identical simulation environment. The variation is in the r direction only.

10.2. Governing Equations and Solution Methodology

The governing equations included in the basic model are shown below.

- Heat transfer equation

$$\rho \cdot Cp \frac{\partial T}{\partial t} + \nabla(-k\nabla T) = Q - \rho \cdot Cp \cdot \vec{u}\nabla T \qquad (10.1)$$

- Mass transfer equation

$$\frac{\partial c_i}{\partial t} + \nabla(-D_{AB}\nabla c_i) = r_i - \vec{u}\nabla c_i \qquad (10.2)$$

- Rate equation

$$ri = -A \times e^{(-\frac{E}{R \times T})} \times Ci \qquad (10.3)$$

the particle changes the basic physical properties such as density, thermal conductivity, and heat capacity used in the heat transport governing equation. The changes in the physical properties ρ_{OS}, Cp and K of raw material were adopted from the literature [37, 52] and allowed to be changed as the reaction progressed using the following expressions;

- Density of the raw material- function of organic composition (org)

$$\rho os = \frac{\text{Rho\_org} \times \text{Rho\_rock}}{(\text{Org} \times (\text{Rho\_rock} - \text{Rho\_org}) + \text{Rho\_org})} \quad (10.4)$$

- Heat capacity of the raw material- function of oil yield and temperature

$$\text{Cp} = 4186.8383 \times [0.172 + (0.067 + 0.00162 \times \text{Grade\_OS} \times \text{cO}) \times (10^{-3} \times \frac{9}{5} \times \text{T})] \quad (10.5)$$

- Thermal conductivity of the raw material –function of oil yield and temperature

$$K = 1.73074 \times [(a'_1 \times (1 - b'_1 \times \left(\frac{9}{5} \times (T - 273.15) - 53\right) - b'_2 \times \left(\frac{9}{5} \times (T - 273.15) - 53\right)^2 \times \exp(a'_2 \times \text{Grade\_OS} \times \text{cO})] \quad (10.6)$$

a_1', b_1, a_2` and $b_2$` are constants. Three reaction mechanisms were examined- a single step mechanism which does not account for the secondary reactions and a two-step mechanism in which oil produced during the process participates in the secondary reaction. The mass coefficients in the reactions were adopted from the literature and were modified based on the observation in the laboratory [121]. The third mechanism is a multistep mechanism proposed by Burnham and Braun [121] and modified by Bauman and Deo [153] for mass stoichiometric coefficients as to match the mass and elemental balances. The mass coefficients (equation 10-7 to 10-9) are assumed constant, though reaction temperature affects the distribution of product.

Table 10-1 shows the molecular weight (MW) and elements, carbon and hydrogen data for the multistep mechanism. The data up to three decimal points are required to conserve the

mass balance. The mass coefficients were calculated balancing the elements and conserving the mass. The products of the primary reaction from kerogen decomposition are classified as HO (heavy oil), LO (light oil), Gas, Char and Methane. Methane is not included in the Gas fraction and does not go through the secondary processes. All other products participate in further pyrolysis and produce solid and fluid products by cracking or coking.

- Single step mechanism

$$\text{Kerogen} \longrightarrow 0.63\ \text{Oil} + 0.24\ \text{Gas} + 0.13\ \text{Coke} \tag{10.7}$$

- Two step mechanism

$$\begin{aligned} \text{Kerogen} &\longrightarrow 0.63\ \text{Oil} + 0.24\ \text{Gas} + 0.13\ \text{Coke} \\ \text{Oil} &\longrightarrow 0.80\ \text{Gas} + 0.20\ \text{Coke} \end{aligned} \tag{10.8}$$

- Multistep mechanism

$$\begin{aligned} \text{Kerogen} &\longrightarrow a_1\cdot\text{HO} + a_2\cdot\text{LO} + a_3\cdot\text{Gas} + a_4\cdot\text{Char} + a_5\cdot\text{CH}_4 \\ \text{HO} &\longrightarrow b_2\cdot\text{LO} + b_3\cdot\text{Gas} + b_4\cdot\text{Char} + b_5\cdot\text{CH}_4 \\ \text{LO} &\longrightarrow c_3\cdot\text{Gas} + c_4\cdot\text{Char} + c_5\cdot\text{CH}_4 \\ \text{Gas} &\longrightarrow d_4\cdot\text{Char} + d_5\cdot\text{CH}_4 \\ \text{Char} &\longrightarrow e_3\cdot\text{Gas} + e_5\cdot\text{CH}_4 + e_6\cdot\text{Coke} \end{aligned} \tag{10.9}$$

Table 10- 1: Elements and molecular weight data used in constructing the multistep step reaction mechanism.

Component	Kerogen	HO	LO	Gas	Char	Methane	Coke
C	1479.000	31.751	11.189	3.354	1.004	1.000	1.185
H	2220.000	42.818	17.510	11.634	0.546	4.000	0.316
Ratio	1.501	1.349	1.565	3.468	0.544	4.000	0.267
MW	20000.550	424.492	152.034	52.011	12.604	16.042	14.552

The kinetic parameters for kerogen decomposition were taken from Tiwari and Deo [148]. The distributions of activation energy and preexponential factor as decomposition reaction progresses were used for the first step. The kinetic expressions for secondary reactions were fixed, E =200 kJ/mol and A = 1E10 S^{-1}. The heat of the reaction was assigned a value of 370 kJ/kg [154]. All the species concentrations were converted to mass units and the equations were solved keeping the overall mass conserved.

The model was simulated first for a single particle, TGA analysis of a fine powder. The convection terms from heat and mass equations were omitted. To understand the effect of the scale (large size) the model was modified by including flow. Convective heat transfer as well as convective flow of the products was introduced in the governing equations using Darcy's law and the continuity equation assuming fluid follows the ideal gas law. Continuity equations coupled with the Darcy flow generates the velocity data. Ideal gas law was used to account for the change in pressure because of density (ρ) variation. Velocity field (u) is determined by the pressure gradient (∇p), the fluid viscosity (μ), and the structure of the porous medium permeability (K_p).

- Darcy law $$u = \frac{Kp}{\mu} \nabla p \quad (10.10)$$

- Continuity equation $$\frac{\partial}{\partial t}(\rho\varepsilon) + \nabla \cdot (\rho u) = Q_m \quad (10.11)$$

- Ideal gas law $$\rho = \frac{pM}{RT} \quad (10.12)$$

An empirical formula for the porosity generated due to kerogen conversion was used [155]. The relationship of porosity and permeability was established using standard Kozney-Carman equation by assuming the average pore diameter of 50×10^{-6} meter.

- Porosity of oil shale as a function of conversion

$$\varepsilon = 0.003+(0.0146+0.0129\times (\text{Grade\_OS}\times \text{xK})-0.000046 \times (\text{Grade\_OS} \times \text{xK})^2) \quad (10.13)$$

- Permeability of oil shale

$$K_p = D_p^2 \times \varepsilon^3/(150 \times (1- \varepsilon)^2) \quad (10.14)$$

The model was calculated with the physical and chemical conditions mentioned above. The initial and boundary conditions were assigned according to the geometry and simulation conditions. For temperature, the initial condition was room temperature and boundary conditions were the pyrolysis temperatures (isothermal and nonisothermal). The boundary was set at atmospheric pressure. The mesh size in the geometry was generated and optimized for each simulation to achieve fast and reliable results.

Following assumptions were applied to develop the model

- It is assumed that the material was a 30 gal/ton grade oil shale contains 18% organic matter that was uniformly distributed. The physical properties expressions (*ρos, Cp , K*) were reported for this grade in the literature.

- The material was heated in the radial direction and it was assumed that the system is symmetrical with respect to z and theta direction.
- Mass transfer through diffusion was not considered. A very small value 10^{-50} [m^2/s] was used for all the species
- Mass transfer equation was solved for each species involved in the reaction network. Kerogen, char and coke were considered as the solid phase, while the oils and gases were the fluid phase.
- Single phase fluid behavior was applied assuming propane as a model fluid to compute the flux of each species. Model built follows the ideal gas law.

10.3. Model Results and Observations

The model developed was simulated with several conditions. A single particle model was examined for all three mechanisms to understand the kinetics and product distribution. This simulation scheme did not include the convective terms and it used the intrinsic kinetics parameters like in the TGA experiments and in a closed system. Figure 10-3 shows the kerogen decomposition and product formation for a single step mechanism for isothermal (400°C) and nonisothermal (10°C/min) boundary conditions. The two step and multistep mechanisms were simulated for the identical conditions and the results are shown in Figure 10-4 and Figure 10-5, respectively.

It can be observed from the results of single particle simulation that the kinetics used for the kerogen decomposition is able to simulate the process effectively. The kerogen decomposition followed the similar trend as TGA analysis. The products formed are in accordance with the mechanisms and associated mass stoichiometry. The results also suggest the effects of the secondary reactions on the final products. To achieve the

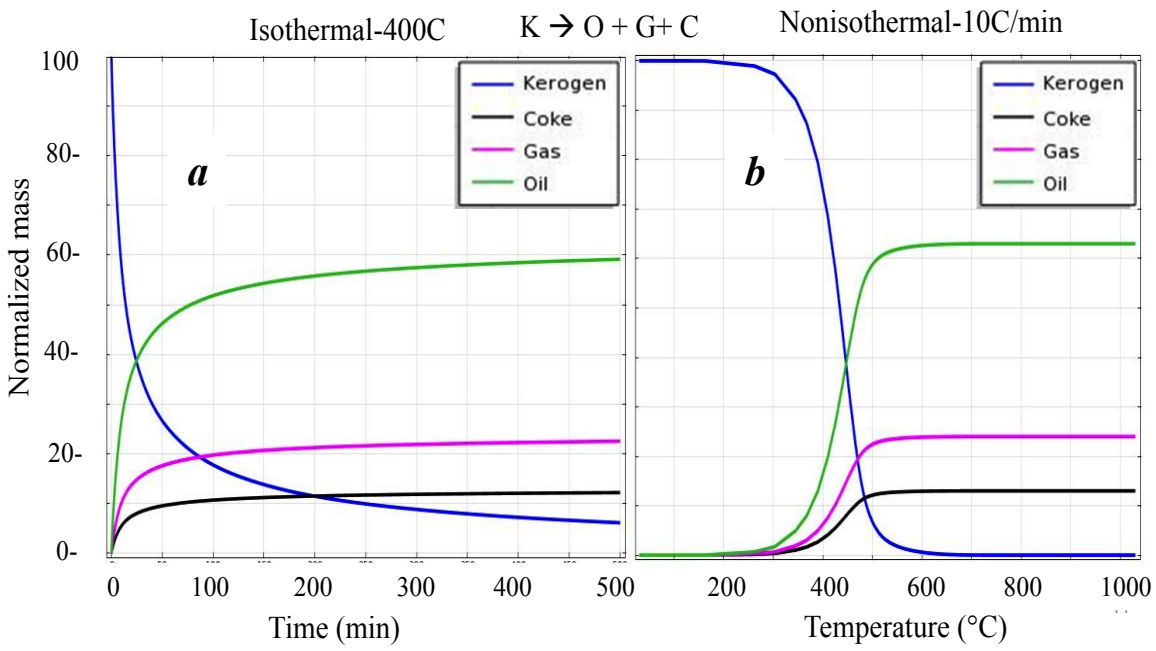

Figure 10- 3: Kerogen decomposition (single particle) and product formation profiles using single step mechanism under (a) isothermal (400°C) and (b) nonisothermal (10°C/min).

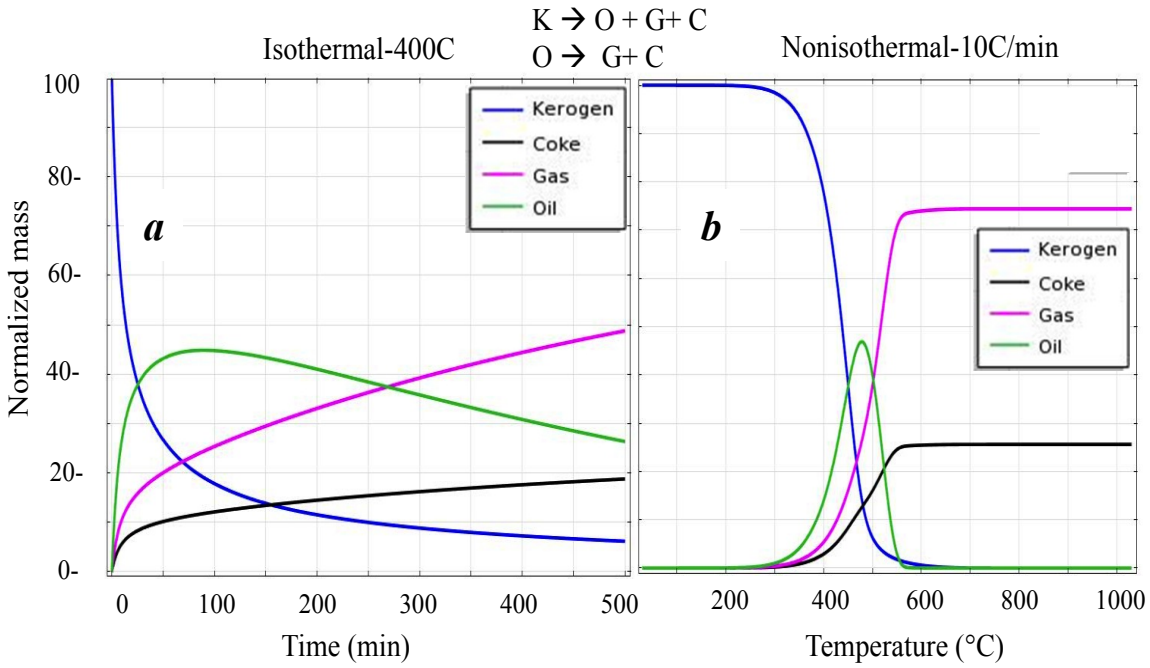

Figure 10- 4: Kerogen decomsposition (single particle) and product formation profiles using two step mechanism under (a) isothermal (400°C) and (b) nonisothermal (10°C/min).

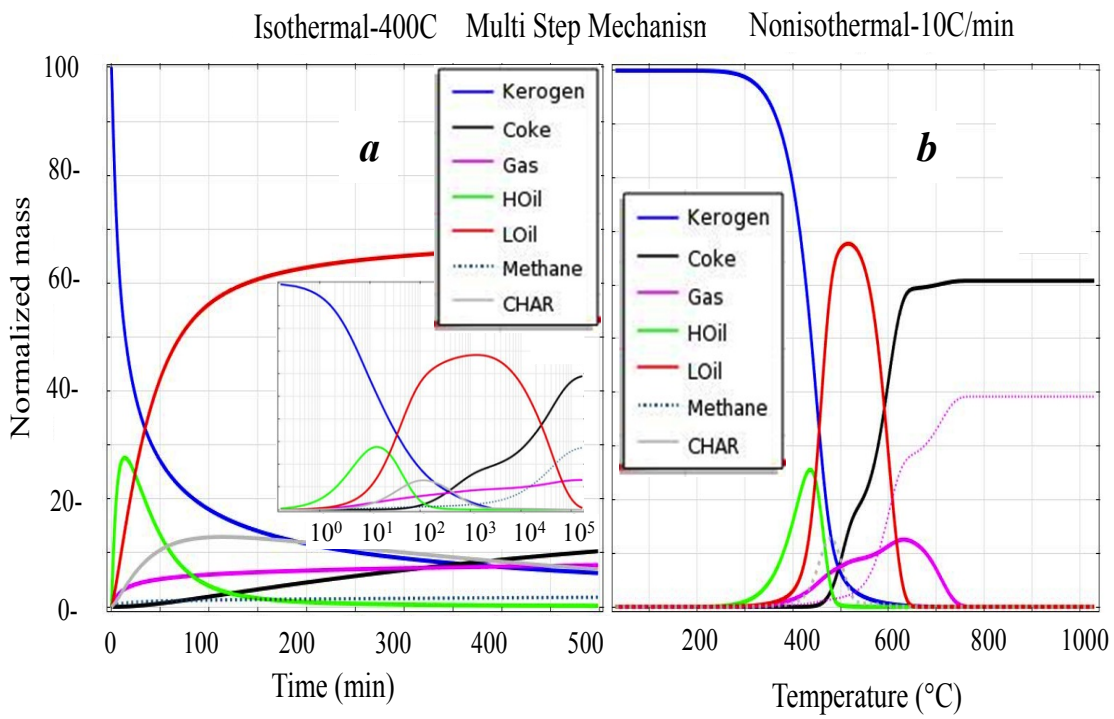

Figure 10- 5: Single particle (TGA scheme in batch mode) of kerogen decomposes to different products using multiple step reactions mechanism under (a) isothermal (400°C) and (b) nonisothermal (10°C/min) pyrolysis. The small window shows the material profiles at long time scale (a log scale).

maximum yield of the desired products, the material needs to be in a pyrolysis environment for a certain time and temperature. Increasing the temperature and heating rate reduced the optimal time. However, it is clear from the results that if the products are heated for a longer time (isothermal) or to higher temperatures (nonisothermal) the final result will be coke and gases. Thus, it is important to sweep the products out.

The reaction mechanism is an important factor to control the product distribution. The multistep mechanisms showed that products are dominated by light oil fractions if the process is shutdown when kerogen decomposition is about 90% at 400°C (isothermal) and 10°C/min (nonisothermal) cases. This value was observed to decrease with an increase in temperature and heating rate for the maximum production of light oil. These are results of the secondary

reactions. The two step mechanism which describes oil degradation as secondary reaction shows that maximum oil yield occurs at 80% and 95% kerogen conversion at 400°C isothermal and 10°C/min nonisothermal conditions respectively.

The next logical step in understanding the product formation rates and distributions was simulating the process with open boundary conditions with a large sample size. The fluid products generated were allowed to travel within the sample by the pressure gradient generated due to gas and methane formation. Core geometry of 10 cm radius was selected. The material was heated in two different configurations which were surface heating and heating from the center of the core. The schematic of the geometries for this simulation scheme is shown in Figure 10-6. In case of heat source at the center of the core a boundary with a radius of 1cm was created inside to act as a heater. There is a temperature distribution across the material in heating schemes. Temperature distribution

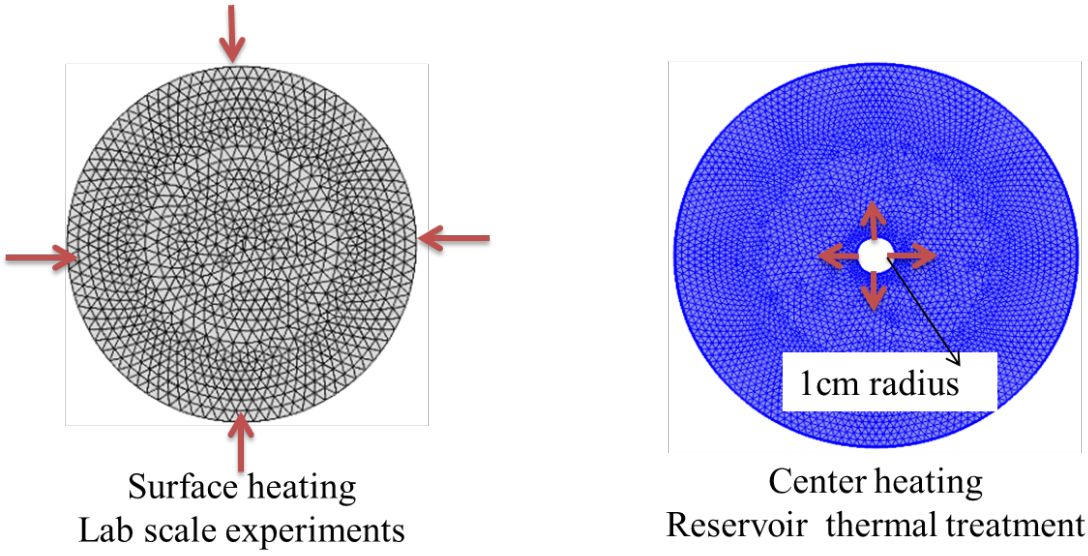

Figure 10- 6: Schematic of the application of the heat to the source material via surface heating and center heating.

controls the kinetics, and hence the product distribution. The temperature distribution across the sample due to heat conduction and resulting rates of heavy oil formation in different sections in case of isothermal (400°C) surface heating are shown in Figure 10-7. The formation and degradation of products occur in a manner similar to single particle simulations. The temperature at the surface is higher thus the formation and degradation of heavy oil occur earlier. And, if the desired products (oils) are not collected at specific time/temperature they participate in the secondary reaction network resulting in formation of more coke and gases.

Further, other physical processes such as convective heat, convective mass transport, and creation of porous media to flow were included in the model. The simulations were carried out when the pressure generated due to the product formation regulated the flow behavior of the fluid products.

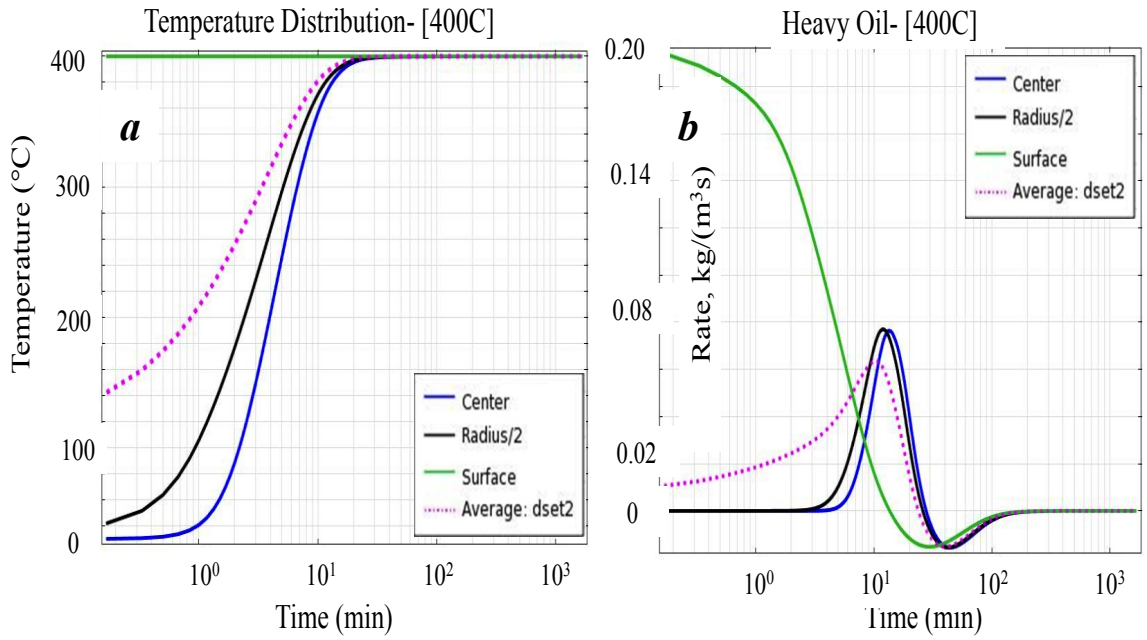

Figure 10- 7: Isothermal (400°C) surface heating, (a) distribution of temperature and (b) rate of heavy oil formation in different sections of the core.

A single phase flow by using propane as a model fluid, for gas and methane fractions with Darcy's law was incorporated in the model. The convection terms in heat and mass equations were included. All fluid products were assumed to follow the velocity of model fluid. The comparison of the rates of product formation at the surface with convection and no convection under nonisothermal heat input at the surface (10°C/min) is shown in Figure 10-8. The rates of fluid products are comparatively higher with convection. This indicates that the convective source in heat and mass transport equations influences the product rates.

When the material is heated from surface, the products form faster at the outer zone and are released. Temperature propagates from the outer surface to inner zone. The product formation creates a porous network. The products at the inner zone form and are transported from a cold to a hot zone. The high temperature in this path favors the secondary reactions, but fluid spends less time due to high porosity. In the case of central

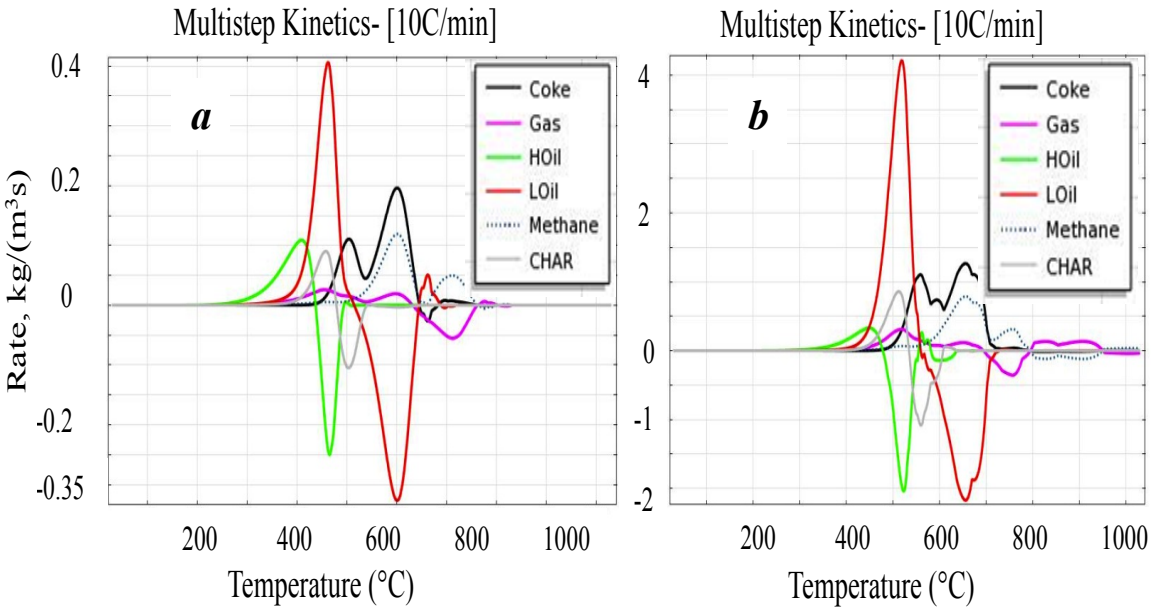

Figure 10- 8: Effect of convection on product formation rates.

heating, the products hit the low temperature and less permeable zone. These conditions restrict the flow and products spend more time within the sample. The condensation reactions due to local thermodynamic conditions may occur. The thermodynamic behavior of the fluid products is not taken into consideration in this model. In both the cases, kinetic conversion experienced a combined isothermal and nonisothermal temperature history. Figure 10-9 shows the average total flux (kg/m^2.s) of the fluid products from the surface of 10cm radius core samples in the surface heating and center heating schemes under isothermal (400°C) heat supply to the material. The comparison of these two plots shows that due to different time/temperate history the material is exposed, average outward fluxes of the products from the surface varies significantly in the distribution. In case of the center heating products come out with a time delay and lighter oil is produced.

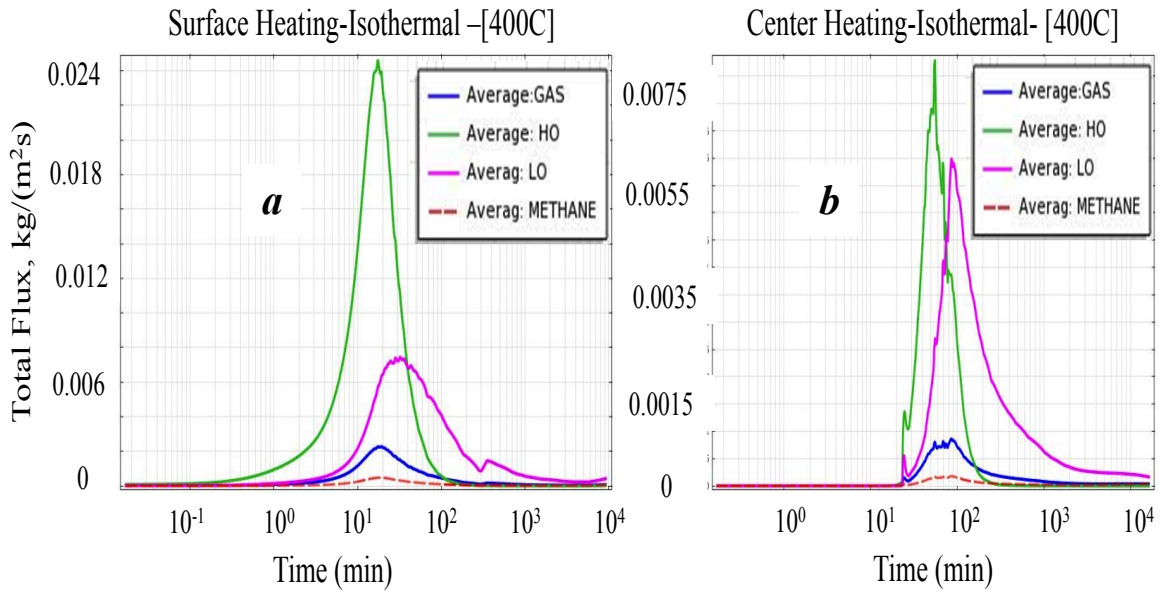

Figure 10- 9: Average total flux of the fluid products from the surface of the core during (a) surface heating and (b) center heating schemes.

10.4. Summary of the Model Results

The model is able to capture the effect of operation conditions and influence of secondary reactions on the distribution of products. The secondary reactions of coking and cracking in the product phase were addressed and their formation kinetics were included. The product distribution is constrained by elemental and product mass balances. The model is capable of predicting compositional information for generated and collected products at different scales. The simulation was designed to understand the effects of the temperature and heating rate on product distribution when additional physics involved in the process are applied. Surface and center heating schemes replicate two different boundary conditions of the core. The heat transfer through a large block experienced both isothermal and nonisothermal behavior simultaneously. The heat distribution regulates the kerogen conversion to product and formation rates. The secondary reactions in the process control the final product distribution. Each physical and chemical process included in this study influences the results. Additional processes which are not considered in this model may alter the product distribution such as thermodynamics of the phase equilibria, multiphase flow behavior, contributions of mineral reactions to the reaction network and the gas pressure generation, etc. The measurement study of the fracture and expansion during the pyrolysis at various temperature and compressive loads was reported [156-158]. These physical processes may also be important in developing a model. The model needs validation against experimental data.

REFERENCES

[1] George JH, Harris HG. Mathematical modeling of insitu oil shale retorting. Siam J Number Anal 1977;14.

[2] Bartis JT, LaTourrette T, Dixon L, Peterson DJ, Cecchine G. OIl shale development in the United States- Prospective and policy issues. In: Rand Corporation, Santa Monica, CA, 2005.

[3] Engler C. Die chemie und physik des erdols. Das Erdol 1913;1:1-37.

[4] ZNuttall HE, Guo T, Schrader S, Thakur DS. Pyrolysis kinetics of several key world oil shales. In: F.P. Miknis, J.F. McKay (Eds.) Geochemistry and chemistry of oil shales, American Chemical Society;1983, p. 269-300.

[5] Burham AK, Richardson JH, Coburn TT. Pyrolysis kinetics for western and eastern oil shale. In proceedings of the 17th intersociety energy conversion engineering conference, IEEE publishing: New York, 1982, pp. 912-7.

[6] Torrente MC, Galan MA. Kinetics of the thermal decomposition of oil shale from puertollano (Spain). Fuel 2001;80:327-34.

[7] Burnham AK. Oil evolution from a self purging reactor: Kinetic and composition at 2C/min and 2C/h. Energy Fuels 1991;5:205-14.

[8] Charlesworth JM. Oil shale pyrolysis. 1. Time and temperature dependence of product composition. Ind Eng Chem Process Des Dev 1985;24:1117-25.

[9] Burnham AK, Singleton MF. High-pressure pyrolysis of green river oil shale. in: F.P. Miknis, J.F. McKay (Eds.) Geochemistry and Chemistry of Oil Shales;1983, p. 335-51.

[10] Sohn HY, Yang HS. Effect of reduced pressure on oil shale retorting. 1. Kinetics of oil generation. Ind Eng Chem Process Des Dev 1985;24:265-70.

[11] Yang HS, Sohn HY. Mathematical analysis of the effect of retorting pressure on oil yield and rate of oil generation from oil shale. Ind Eng Chem Process Des Dev 1985;24:274-80.

[12] Stainforth JG. Practical kinetic modeling of petroleum generation and expulsion. Mar Petrol Geol 2009;26:552-72.

[13] Burnham AK, Happe JA. On the mechanism of kerogen pyrolysis. Fuel 1984;63:1353-6.

[14] Burnham AK. Relationship between hydrous and ordinary pyrolysis. In: NATO advanced study institute on composition, geochemistry and conversion of oil shales conference Akcay, Turkey, 1995 pp. 211–28.

[15] Pan C, Geng A, Zhong N, Liu J, Yu L. Kerogen pyrolysis in the presence and absence of water and minerals. 1. Gas components. Energy Fuels 2008;22:416-27.

[16] Lewan MD, Ruble TE. Comparison of petroleum generation kinetics by isothermal hydrous and non-isothermal open system pyrolysis. Org Geochem 2002;33:1457-75.

[17] Michels R, Landaisa P, Torkelsonb BE, Philpc RP. Effects of effluents and water pressure on oil generation during confined pyrolysis and high pressure hydrous pyrolysis. Geochim Cosmochim Acta 1995;59:1589-604.

[18] Hill GR, Johnson DJ, Miller L, Dougan JL. Direct production of low pour point high gravity shale oil. Ind Eng Chem Prod Res Dev 1967;6:52-9.

[19] Haung ETS. Retorting of single oil shale blocks with nitrogen and air. Soc Petrol Eng J 1977;17:331-6.

[20] Jaber JO, Probert SD. Nonisothermal thermogravimetry and decomposition kinetics of two Jordian oil shales under different processing conditions. Fuel Process Technol 2000;63:57-70.

[21] Kavianian HR, Yesavage VF, Dickson PF, Peters RW. Kinetic simulation model for steam pyrolysis of oil shale feedstock. Ind Eng Chem Res 1990;29:527-34.

[22] Fathoni AZ, Batts BD. A literature review of fuel stability studies with a particular emphasis on shale oil. Energy Fuels 1992;6:681–93.

[23] A technical, economical and legal assesment of North American heavy oil, oil sands, and oil shale resources; In responce to Energy Policy Act of 2005 Section 369(p); Prepared by Utah heavy oil program, 2007.

[24] Survey of energy resources. In: World Energy Council, 2007, pp. 93-115.

[25] Smith JW. Oil shale resources of the United States. CSM Mineral and Energy Resources Series 1980;23.

[26] Dyni JR. Geology and resources of some world oil shale deposits. Oil Shale 2003;20:193-252.

[27] Campbell JH, Kokinas GJ, Stout ND. Kinetics of oil generation from Colorado oil shale. Fuel 1978;57:372-6.

[28] VandenBerg MD. Basin wide evaluation of the uppermost green river formation's oil shale resource, Unita Basin, Utah and Colorado. In: Utah Geological Survey, 2008.

[29] Heistand RN. The Fishcer Assay, a standard method? in: Symposium on oil shale, tar sands, and related materials- production and utilization of sinfuels, San Francisco, 1976.

[30] Wellington SL, Berchenko IE, P. RE, Fowler TD, Ryan RC, Shalin GT, Stegemeier GL, Vinegar HJ. U.S. Patent 6,880,633, 2005.

[31] Symington WA, Olgaard DL, Phillps TC, Thomas MM, Yeakel JD. ExxonMobile's electrofrac™ process for in situ oil shale conversion. In: 26th Oil Shale Symposium, Colorado Energy Research Institute, Colorado, 2006.

[32] Kasevich RS, Kolker M, Dwyer AS. U.S. Patent 4,140,179, 1979.

[33] Hubbard AB, Robinson WE. A thermal decomposition study of Colorado oil shale. in, U.S. Bureau of Mine:Report of investigation #4744, 1954.

[34] Pan Z, Feng HY, Smith JM. Rates of pyrolysis of colorado oil shale. AIChE J 1985;31:721-8.

[35] Allred VD. Kinetics of oil shale pyrolysis. Chem Eng Prog 1966;62:55-60.

[36] Braun RL, Rothman AJ. Oil shale pyrolysis: Kinetics and mechanism of oil production. Fuel 1975;54:129-31.

[37] Gregg ML, Campbell JH, Taylor JR. Laboratory and modelling investigation of a Colorado oil shale block heated to 900C. Fuel 1981;60:179-88.

[38] McKee RH, Lyder EE. Thermal decomposition of shales. Ind and Eng Chem 1921;13:613-8.

[39] Maier CG, Zimmerly SR. The chemical dynamics of the transformation of organic matter to bitumen in oil shale. Utah Eng Exper Sta Bull 1924;14:62-81.

[40] Franks AJ, Goodier BD. Preliminary study of the organic matter of Colorado oil shales. Quarterly of the Colorado School of Mines 1922;17:3-16.

[41] Bae JH. Some effects of pressure on oil shale retorting. Soc Petrol Eng J 1969;9:287-92.

[42] Parker JC, Zhang F. Efficient formulation of heat and mass transfer in oil shale retort models. In: 26th Oil Shale Symposium, Coloarodo School of Mines, 2006.

[43] Rajeshwar K, Nottenburg N, Dubow J. Review: Thermophysical properties of oil shales. J Mater Sci 1979;14:2025-52.

[44] Fausett DW, Mikinis FP. Simplified kinetics of oil shale pyrolysis. In: Colorado School of Mines Press, Golden, CO;1981.

[45] Campbell JH. The kinetics of decomposition of Colorado oil shale II. Carbonate minerals. Lawrence Livermore Laboratory Rep 1978;UCRL-52089-2.

[46] Jeong KM, Patzer IJF. Indigenous mineral matter effects in pyrolysis of Green River oil shale. In: F.P. Miknis, J.F. McKay (Eds.) Geochemistry and Chemistry of Oil Shales, Americal Chemical Society;1983, p. 529–42.

[47] Marshall CP, Kannangara GSK, Wilson MA, Guerbois JP, Hartung-Kagi B, Hart G. Potential of thermogravimetric analysis coupled with mass spectrometry for the evaluation of kerogen in source rocks. Chem Geol 2002;184:185-94.

[48] Galan MA, Smith JM. Pyrolysis of oil shale: Experimental study of transport effects. AIChE J 1983;29:604-10.

[49] Charlesworth JM. Oil shale pyrolysis. 2. Kinetics and mechanism of hydrocarbon evolution. Ind Eng Chem Process Des Dev 1985;24:1125-32.

[50] Burnham AK, Ward RL. A possible mechanism of alkene/alkane production. in: H.C. Stauffer (Ed.) Oil Shale, Tar Sands, and Related Materials, American Chemical Society, Washington DC;1981, p. 79-92.

[51] Burnham AK. Chemistry of shale oil cracking. in: H.C. Stauffer (Ed.) Oil Shale, Tar Sands, and Related Materials, American Chemical Society, Washington DC;1981, p. 79-92.

[52] Campbell JH, Koskians GJ, Coburn TT, D.Stout N. Oil shale retorting: The effects of particle size and heating rate on oil evolution and intraparticle oil degradation. InSitu 1978;2:1-47.

[53] Rajeshwar K. The kinetics of the thermal decomposition of green river oil shale kerogen by nonisothermal thermogravimetry. Thermochim Acta 1981;45:253-63.

[54] Hillier J, Fletcher J, Orgill J, Isackson C, Fletcher TH. An improved method for determination of kinetic parameters from constant heating rate TGA oil shale pyrolysis data. Am Chem Soc, Div Fuel Chem 2009;54:155-7.

[55] Li S, Yue C. Study of pyrolysis kinetics of oil shale. Fuel 2003;82:337-42.

[56] Li S, Yue C. Study of different kinetic models for oil shale pyrolysis. Fuel Process Technol 2003;85:51-61.

[57] Qing W, Baizhong S, Aijuan H, Jingru B, Shaohua L. Pyrolysis charactristic of Huadian oil shale. Oil Shale 2007;24:147-57.

[58] William PT, Ahmad N. Influence of process conditions on the pyrolysis of Pakistani oil shale. Fuel 1999;78:653-62.

[59] Thakur DS, Nuttal HE. Kinetics of pyrolysis of Moroccan oil shale by thermogravimetry. Ind Eng Chem Process Des Dev 1987;26:1351-6.

[60] Shin SM, Sohn HY. Nonisothermal determination of the intrinsic kinetics of oil generation from oil shale. Ind Eng Chem Process Des Dev 1980;19:420-6.

[61] Campbell JH, Koskinas GH, D SN. Kinetics of oil generation from Colorado oil shale Fuel 1978;57:372-6.

[62] Leavitt DR, Tyler AL, Kafesjiant AS. Kerogen decomposition kinetics of selected green river and eastern U.S. oil shales from thermal solution experiments. Energy Fuels 1987;1:520-5.

[63] Brown ME, Maciejewski M, Vyazovkin S, Nomen R, Sempere J, Burnham A, Opfermann J, Strey R, Anderson HL, Kemmeler A, Janssens J, Desseyn HO, Li CR, Tang TB, Roduit B, Malek J, Mitsuhasshi T. Computational aspects of kinetic analysis: Part A: The ICTAC kinetics project data, methods and results. Thermochim Acta 2000;355:125-43.

[64] Burnham AK. Computaional aspects of kinetic analysis. Part D: The ICTAC kinetic project multi thermal history model fitting methods and their relation to isoconversion methods in: Thermochim. Acta, 2000, pp. 165-70.

[65] Maciejewski M. Computational aspects of kinetic analysis: Part B- The ICTAC project- The decomposition kinetics of calcium carbonate revisited, or some tips on survival in the kinetic minefield. Thermochim Acta 2000;355:125-43.

[66] Roudit B. Computational aspects of kinetic analysis: Part E- Numerical techniques and kinetics of solid state processes. Thermochim Acta 2000;35:171-80.

[67] Vyazovkin S. Computational aspects of kinetic analysis: Part C- The ICTAC project- The light at the end of the tunnel? Thermochim Acta 2000;355:155-63.

[68] Burnham AK, Braun RL. Global kinetic analysis of complex materials. Energy Fuels 1999;13:1–22.

[69] Burnham AK, Dinh LN. A comparision of isoconversional and model fitting kinetic parameter estimation and application predictions. J Therm Anal Calorim 2007;89:479-90.

[70] Vyazovkin S. Reply to “What is meant by the term ‘variable activation energy’ when applied in the kinetics analyses of solid state decompositions (crystolysis reactions)?”. Thermochim Acta 2003;397:269-71.

[71] Burnham AK. Chemistry and kinetics of oil shale retorting. In: Oil shale: A solution to the liquid fuel dilemma, ACS symposium series;2010, p. 115–34.

[72] Braun RL, Burnham AK. Analysis of chemical reaction kinetics using a distribution of activation energies and simpler models. Energy Fuels 1987;1:153-61.

[73] Burnham AK, Braun RL. General kinetic model of oil shale pyrolysis. InSitu 1985;9:1-23.

[74] Burnham AK, Braun RL, Coburn TT, Sandvik EI, Curry DJ, Schmidt BJ, Noble RA. An appropriate kinetic model for well-preserved algal kerogen. Energy Fuels 1996;10:49-59.

[75] Starink MJ. The determination of activation energy from linear heating rate experiments: A comparison of the accuracy of isoconversion methods. Thermochim Acta 2003;404:163-76.

[76] Sundararaman P, Merz PH, Mann RG. Determination of kerogen activation energy distribution. Energy Fuels 1992;6:793-803.

[77] Al-Ayed OS, Matouq M, Anbar Z, Khaleel AM, Abu-Nameh E. Oil shale pyrolysis kinetics and variable activation energy principle. Appl Energ 2010;87:1269-72.

[78] Friedman HL. Kinetics of thermal degradation of charforming plastics from thermogravimetry. In: Application to a phenolic plastic. J Polym SciPart C 1964;6:183–95.

[79] Vyazovkin S, Wight CA. Estimating realistic confidence intervals for the activation energy determined from thermoanalytical measurements. Anal Chem 2000;72:3171-5.

[80] Vyazovkin S, Wight CA. Isothermal and nonisothermal kinetics of thermally stimulated reactions of solids. Int Rev Phys Chem 1998;17:407-33.

[81] Vyzovkin SV, Lesnikovich AL. Practical application of isoconversional methods. Thermochim Acta 1992;203:177-85.

[82] Vyazovkin S, Wight CA. Kinetics in solids. Annu Rev Phys Chem 1997;48:125-49.

[83] Espitalie J, Ungerer P, Irwin I, Marquis F. Primary cracking of kerogens. Experimenting and modeling C_1, C_2–C_5, C_6–C_{15} and C_{15}+ classes of hydrocarbons formed. Org Geochem 1988;13.

[84] Huizinga BJ, Aizenshtat ZA, Peters KE. Programmed pyrolysis gas chromatography of artificially matured Green River kerogen. Energy Fuels 1988;2:74-81.

[85] Morandi JR, Jensen HB. Comparison of porphyrins from shale oil, oil shale, and petroleum by absorption and mass spectroscopy. J Chem Eng Data 1966;11:80-8.

[86] Wood KV, Narayan R, Stringham KR, Huang SL, Leehe H. Characterization of the oil extract of an Indiana shale. Fuel Process Technol 1990;26:73-81.

[87] Lee S. Oil shale technology. CRC Press Inc, Boca Raton, Florida, USA; 1991.

[88] Greenwood PF, George SC. Mass spectral characteristic of C_{19} and C_{20} tricylcic terpanes detected in Latrobe Tasmanite oil shale. Eur J Mass Spectrom 1999;5:221-30.

[89] Steck SJ, Muenow DW, Margrave JL. Mass spectrometric volatilization studies of oil shale. in: Division of Fuel Chemistry, American Chemical Society, Chicago, 1970.

[90] Chakravarty T, Windig W, Taghizadeh K, Meuzelaar HLC, Shadle LJ. Computer-assisted interpretation of pyrolysis mass spectra of two oil shales and their corresponding kerogens. Energy Fuels 1988;2:191-6.

[91] Campbell JH, Kokinas GJ, Gallegos G, Gregg M. Gas evolution during oil shale pyrolysis 1: Nonisothermal rate measurements. Fuel 1980;59:718-26.

[92] Campbell JH, Gallegos G, Gregg M. Gas evolution during oil shale pyrolysis 2: Kinetic and stoichiometric analysis. Fuel 1980;59:727-32.

[93] Huss EB, Burnham AK. Gas evolution during pyrolysis of various Colorado oil shales. Fuel 1982;61:1188-96.

[94] Burnham AK, Huss EB, Singleton MF. Pyrolysis kinetics for Green River oil shale from the saline zone. Fuel 1983;62:1199-204.

[95] Oh MS, Coburn TT, Crawford RW, Burnham AK. Study of gas evolution during oil shale pyrolysis by TQMS. Lawrence Livermore National Laboratory, UCRL 98233, 1988.

[96] Reynolds JG, Crawford RW, Burnham AK. Analysis of oil shale and petroleum source rock pyrolysis by triple quadrupole mass spectrometry: Comparisons of gas evolution at the heating rate of 10^0C/min. Energy Fuels 1991;5:507-23.

[97] Burnham AK, Braun RL, Gregg HR, Samoun AM. Comparison of methods for measuring kerogen pyrolysis rates and fitting kinetic parameters. Energy Fuels 1987;1:452-8.

[98] Burnham AK, Samoun AM, Reynolds JG. Characterization of petroleum source rocks by pyrolysis-mass spectroscopy gas evolution profiles. Lawrence Livermore National Laboratory, UCRL 111012, 1992.

[99] Burnham AK. Pyrolysis kinetics for the Bakken shale. Lawrence Livermore National Laboratory, UCRL 109622, 1992.

[100] Braun RL, Burnham AK, Reynolds JG. Oil and gas evolution kinetics for oil shale and petroleum source rocks determined from pyrolysis-TQMS data at two heating rates. Energy Fuels 1992;6:468-74.

[101] Oh MS, Taylor RW, Coburn TT, Crawford RW. Ammonia evolution during oil shale pyrolysis. Energy Fuels 1988;2:100-5.

[102] Oh MS, Fostera KG, Alcaraza A, Crawforda RW, Taylora RW, Coburna TT. Thermal decomposition of buddingtonite in oil shales. Fuel 1993;72:517-23.

[103] Wong CM, Crawford RW, Burnham AK. Determination of sulfur-containing gases from oil shale pyrolysis by triple quadrupole mass spectrometry. Anal Chem 1984;56:390-5.

[104] Wong CM, Crawforda RW. Application of a self-adaptive detector system on a triple quadrupole MS/MS to high explosives and sulfur-containing pyrolysis gases from oil shale. Int J Mass spectrom 1984;60:107-16.

[105] Meuzelaa HLC, Windig W, Futrell JH, Harper AM, Larter SR. Pyrolysis mass spectrometry and multivariable analysis of several key world oil shale kerogens and some recent alginites. In: T. Aczel (Ed.) Mass Spectrometric Characterization of Shale Oils: A Symposium;1986, p. 81-108.

[106] Khan MR. Influence of weathering and low-temperature preoxidation on oil shale and coal cevolatilization. Energy Fuels 1987;1:366-76.

[107] Stout ND, Koskinas GJ, Raley JH, Santor JD, Opila RL, Rothman AJ. Pyrolysis of oil shale, the effects of thermal history on oil yiled. In: 9th Oil Shale Symposium, Colorado School of Mines, 1976, pp. 153-72.

[108] Miknis FP, Maclel GE. In: 14th Oil Shale Symposium, 1981, pp. 270.

[109] Nazzal JM. Influnce of heating rate on the pyrolysis of Jordon oil shale. J Anal Appl Pyrolysis 2002;62:225-38.

[110] Nazzal JM. The influence of grain size on the products yiled and shale oil composition from the pyrolysis of Sultani oil shale. Energy Convers Manage 2008;49:3278-86.

[111] Litster J, Newell RB, Bhell PRF. Pyrolysis of Rundle oilshale in a continuous fluidized bed retort. Fuel 1988;67:1327-30.

[112] Yang HS, Sohn HY. Effect of reduced pressure on oil shale retorting. 2. Oil yield. Ind Eng Chem Process Des Dev 1985;24:271-3.

[113] Noble RD, Harris HG, Tucker WF. Isothermal oil shale pyrolysis. 2. Kinetic of product formation and composition at various pressure. Fuel 1981;60:573-6.

[114] Voge HH, Good GM. Thermal cracking and high paraffins. J Am Chem Soc 1949;71:593.

[115] Hillier JL, Fletcher TH. Pyrolysis kinetics of a Green River oil shale using a pressurized TGA. Energy Fuels 2011;25:232-9.

[116] Symington WA, Spiecker PM. Heat conduction modeling tools for screening insitu oil shale conversion processes. In: 28th Oil Shale Symposium, Colorado School of Mines, Colorado, 2008.

[117] Computer Modeling Group. STARS User Manual. 2007.

[118] Huang CK. Development of a general thermal oil reservoir simulator under a modularized framework. In: University of Utah, Salt Lake City, Utah, 2009.

[119] Granoff B, Nuttall HE. Pyrolysis kinetics for oil Shale particles Fuel 1977;56.

[120] Braun RL, Burnham AK. Mathematical model of oil generation, degradation, and expulsion. Energy Fuels 1990;4:132-46.

[121] Braun RL, Burnham AK. PMOD: A flexible model of oil and gas generation, cracking and expulsion. In: 15th International Metting on Organic Geochemistry, Manchester, England, 1991.

[122] Braun RL, Burnham AK. Chemical reaction model for oil and gas generation from type I and II kerogens. LLNL 1993.

[123] Stainforth JG. Practical kinetic modeling of petroleum generation and expulsion. Marine and Petroleum Geology 2009;26:552-72.

[124] Coburn TT, Oh MS, Crawford RW, Foster KG. Water generation during pyrolysis of oil shale. 1. Sources. Energy Fuels 1989;3:216-23.

[125] ASTM E1582-04 Standard Practice for Calibration of Temperature Scale for Thermogravimetry. ASTM International.

[126] Neer LA, Deo MD. Simulated distillation of oils with a wide carbon number distribution. J Chromatogr Sci 1995;33:133-8.

[127] ASTM D5307-97, Standard test method for determination of boiling range distribution of crude oils by gas chromatography. ASTM International 2002.

[128] Roehner RM, Hanson FV. Determination of wax precipitation temperature and amount of precipitated solid wax versus temperature for crude oils using FTIR spectroscopy. Energy and Fuels 2001;15:756—63.

[129] ASTM D1298-99, Standard test method method for density, relative density (specific gravity), or API gravity of crude petroleum and liquid petroleum products by hydrometer methods. ASTM International.

[130] ASTM D1217-93, Standard test method for density, relative density (Specific gravity) of liquids by Bingham pycnometer. ASTM International.

[131] ASTM D4052-96, Standard test method for density and relative density of crude oils by digital density analyzer. ASTM International.

[132] ASTM D5002-99, Standard test method for density and relative density of crude oils by digital density analyzer. .

[133] ASTM D2983-04, Standard test method for low-temperature viscosity of lubricants measured by brookfield viscometer. ASTM International.

[134] Hutton A, Bharati S, Robl T. Chemical and petrographical classification of kerogen/macerals. Energy Fules 1994;8:1478-88.

[135] Araújo HD, Silva NFD, Acchar W, Gomes UU. Thermal decomposition of illite. Mat Res 2004;7:359-61.

[136] Johnsona DR, Younga NB, Robb WA. Thermal characteristics of analcime and its effect on heat requirements for oil shale retorting. Fuel 1975;54:249-52.

[137] Behar F, Vandenbroucke M. Chemical modelling of kerogens. Org Geochem 1987;11:15-24.

[138] Vandenbroucke M, Largeau C. Kerogen origin, evaluation and structure. Org Geochem 2007;38:719-833.

[139] Blazek A. Thermal analysis. In: J.F. Tyson (Ed.) Thermal analysis, Van Nostrand Reinhold, London;1973.

[140] Vyazovkin S, A LL. Estimation of the pre-exponential factor in the isoconversional calculation of effective kinetic parameters. Thermochimica Acta 1988;128:297-300.

[141] Vyazovkin S, Linert W. Detecting isokinetic relationships in nonisothermal systems by the isoconversional method Thermochim Acta 1995;269/270:61-72.

[142] Vyazovkin S, Sbirrazzuoli N. Confidence intervals for the activation energy estimated by few experiments. Anal Chim Acta 1997;355:175-80.

[143] Doyle CD. Estimating isothermal life from thermogravimetric data. J Appl Polym Sci 1962;6:639-42.

[144] Senum GI, Yang RT. Rational approximations of the integral of the Arrhenius function. J Therm Anal Calorim 1977;11:445-7.

[145] Constable FH. The mechanism of catalytic decomposition. In: Proceedings of the Royal Society of London, The Royal Society, 1923, pp. 355-78.

[146] Boudreau BP, Ruddick BR. On a reactive continuum representation of organic matter diagenesis. Am J Sci 1991;291:507-38.

[147] Lakshmanan CC, White N. A new distributed activation energy model using weibull distribution for the representation of complex kinetics. Energy Fuels 1994;8:1158-67.

[148] Tiwari P, Deo M. Detailed kinetic analysis of oil shale pyrolysis TGA data. AIChE J 2011;57: n/a. doi: 10.1002/aic.12589.

[149] Galan MA, Smith JM. Pyrolysis of oil shale: Experimental study of transport effects. AIChE 2006 Spring National Meeting 1983;29.

[150] Brown ME, Maciejewski M, Vyazovkin S, Nomen R, Sempere J, Burnham A, Opfermann J, Strey R, Anderson HL, Kemmeler A, Janssens J, Desseyn HO, Li CR, Tang TB, Roduit B, Malek J, Mitsuhasshi T. Computational aspects of kinetic analysis: Part A-The ICTAC kinetics project-data, methods and results. Thermochim Acta 2000;355:125-43.

[151] Lewan MD. Water as a source of hydrogen and oxygen in petroleum formation by hydrous pyrolysis. Amer Chem Soc Div Fuel Chem 1992;37:1643-49.

[152] Vandergrift GF, Winans RE, Scott RG, Horwitz EP. Quantitative study of the carboxylic acids in Green River oil shale Bitumen. Fuel 1980;59:627-33.

[153] Bauman JH, Deo MD. Parameter space reduction and sensitivity analysis in complex thermal subsurface production processes. Energy Fuels 2011;25:251-9.

[154] Camp DW. Oil shale heat capacity relations and heats of pyrolysis and dehydration. LLNL. In: 20th Oil shale symposium, Golden, CO, 1987.

[155] Baughman GL. Synthetic fuels data handbook : U.S. oil shale, U.S. coal, oil sands. Denver : Cameron Engineers 1978

[156] Duvall EWF, Sohn HY, Pitt CH. Physical behaviour of oil shale at various temperatures and compressive loads: 2. Thermal expansion under various loads. Fuel 1985;64:184-8.

[157] Duvall EWF, Sohn HY, Pitt CH. Physical behaviour of oil shale at various temperatures and compressive loads: 3. Structure failure under loads. Fuel 1985;64:938-40.

[158] Duvall EWF, Sohn HY, Pitt CH, Bronson MC. Physical behavior of oil shale at various temperatures and compressive loads: 1. Free thermal expansion. Fuel 1983;62:1455-61.

[159] Chen WJ, Nuttall HE. Paper presented at the 86th AIChE National Meeting, Houston, Texas. 1979.

[160] Coats AW, Redfern JP. Kinetic parameters from thermodynamic data. Nature (London) 1964;201:68-9.

[161] Kissinger HE. Reaction kinetics in differential thermal analysis. Anal Chem 1957;29:1702-6.

Three-Dimensional Structure of the Siskin Green River Oil Shale Kerogen Model: A Comparison between Calculated and Observed Properties

Anita M. Orendt,[1] Ian S.O. Pimienta,[1,2] Shyam R. Badu,[1] Mark S. Solum,[3] Ronald J. Pugmire,[4] and Julio C. Facelli[1,5]

[1]Center for High Performance Computing and [3]Departments of Chemistry, [4]Chemical and Fuels Engineering, and [5]Biomedical Informatics University of Utah, Salt Lake City, Utah 84112

[2]Department of Chemistry and Physics, Troy University, Troy, Alabama 36082

Darren R. Locke,[6] Karena W. Chapman,[6] Peter J. Chupas,[6] and Randall E. Winans[6]

[6]X-ray Science Division, Advanced Photon Source, Argonne National Laboratory, 9700 S. Cass Avenue, Lemont, Illinois 60439

Abstract

Three-dimensional (3D) structural models of the Green River kerogen based on the two-dimensional (2D) structure proposed by Siskin were generated using a combination of *ab initio* and molecular mechanics calculations. Several initial monomer conformations were generated using the simulated annealing procedure, followed by minimization via quantum mechanical calculations. ^{13}C solid state nuclear magnetic resonance (SSNMR) spectra and pair distribution function (PDF) plots were calculated based on these 3D models and compared to experimental results obtained on a Green River kerogen sample. The results show reasonable good agreement between calculated and experimental results.

Introduction

Kerogen is defined as the insoluble organic component of the organic matter in sedimentary rocks. This organic matter is usually mixed with minerals during its deposition which contributes to the difficulty in its physical isolation. Kerogen is not soluble in normal organic solvents because of the large molecular weight up to several thousand Daltons.[1–4] Kerogen is found in rocks such as shale, as oil shale deposits and upon heating in the Earth's crust, some types release hydrocarbons in the form of crude oil or natural gas.

As kerogen is a mixture of organic material, its chemical composition varies from one sample to another. According to the van Krevelen diagram, kerogens can be classified based on the ratios of H/C and O/C.[5] Type I kerogens have H/C ratio greater than 1.25 and O/C ratio less than 0.15. This class is derived primarily from cyanobacteria or various Chlorophyta and dinoflagellates. Type II kerogens, derived from marine planktonic organisms, have H/C ratio less than 1.25 and O/C ratio of 0.03 to 0.18. Type II kerogens can be enriched in organic sulfur; in this case they are further classified as belonging to Type IIS kerogens. Type III kerogens are derived primarily from higher plant remains in coals and coaly shales; they possess a low hydrogen count (H/C < 1, O/C ≡ 0.03–0.3) because of the extensive ring and aromatic character in these systems. Finally, type IV kerogens are comprised of mostly polycyclic aromatic hydrocarbons with H/C ratio less than 0.5. They contain mostly decomposed organic matter and have no potential to produce hydrocarbons.

Source rocks in the Green River formation, one of the most extensive oil shale reserves in the world, contains hydrogen-rich algal kerogen (type I) with up to ~20 wt% organic matter in the form of amorphous kerogen solid integrated in a silicate- and carbonate-based mineral matrix.[6,7] In the past few years, investigators have employed different methods to separate organic kerogen from inorganic minerals in oil shales and to recover the unaltered kerogen for characterization studies.[8–10] Although considerable progress has been achieved from these studies, the complete isolation of kerogen from oil shales remain difficult.

In the case of these petroleum precursors, i.e., both the source rocks and the kerogens, little information is presently available to describe their physical behavior.[11] Only a few relevant studies have been published which utilize both chemical and instrumental analysis to reconstruct a stochastic two-dimensional model of kerogens.[12-16] The work of Durand and co-workers dealt with type I and type II kerogens.[12] More recently, two-dimensional (2D) models of kerogen have been proposed by Siskin[13] for type I Green River Oil Shale (GROS) and Lille[14] for kukersite (a type II/I kerogen). A much larger (more than 10^4 core structures with approximately 10^6 atoms), more general 2D kerogen model[16] has also been developed using the data from various solid state analyses to construct the cores; this model has been used to predict oil and gas compositional yields.

A potential solution to aid in the isolation of kerogen is the analysis of its three dimensional (3D) molecular structure using molecular modeling and simulation. Atomistic modeling is routinely used in many industries (pharmaceutical, polymers, coatings, explosives, membrane proteins, etc.) to gain insight to material properties and behavior. Faulon[15] reported some preliminary data on 3D structures of kerogen but there has been a lack of modeling work that utilizes the molecular modeling tools that are

available today. Hence, little is known about the 3D characteristics of any of the kerogen models. The 3D characteristics of kerogen will not only define the manner in which the kerogen folds and interacts with both the extractable bitumen and the mineral matter, but the structural information will provide a new view of the structure and which portions of the structure are exposed on the surface, which portions are accessible through channels, and/or which portions may be isolated in the interior of the structure. An understanding of where the various functional groups are located may serve as useful guides for developing novel processing schemes for resource recovery. In addition, the surface exposure of polar functional groups will provide new information on the interaction of the kerogen structure with the inorganic matrix that appears to bind tightly to the mineral matter.[17-20]

In this work, the 3D structure of the Green River Siskin model[13] was obtained using a combination of *ab initio* and molecular mechanics calculations. The 3D structure was then used to calculate the ^{13}C chemical shifts, from which a simulated ^{13}C spectrum can be generated, as well as to simulate the expected atomic pairwise distribution function (PDF) plot. A PDF plot is gives the probability of finding an atom at a given radial distance from another atom; the peaks observed correspond directly to interatomic distances within the sample and is suitable for this study as it provides local structural information independent of long-range order.[21,22] ^{13}C solid state NMR (SSNMR) is also a powerful tool to obtain structural information on insoluble samples such as kerogens. Using the methodology developed by Grant and Pugmire[23] and used extensively on fossil fuel samples, SSNMR ^{13}C spectra can be analyzed to provide detailed structural data such as the average aromatic cluster size and the average number of substituents on the clusters.[23]

The ^{13}C SSNMR spectrum and PDF plot simulated using our model are compared with their experimental counterparts on the kerogen extracted from a segment of a Green River basin shale core.[24] The comparison of the simulated and experimental properties allows for an evaluation of the quality of the 3D model as well as the underlying 2D one. The existence of a 3D model that has been validated against experimental data will allow for further study on the interaction between the kerogen and the mineral matrix as well as the further processing of the kerogen in oil production process.

Computational and Experimental Details

Generation of 3D Model: A 3D structure corresponding to the 2D Siskin's kerogen model[13] (chemical formula of $C_{645}H_{1017}N_{19}O_{17}S_4$; molecular weight of 9438.35 dalton) was built using HyperChem.[25] A preliminary chemical structure was obtained via the molecular mechanics energy minimization routine in HyperChem using the MM+[26] force field. This minimized structure was further optimized using the *ab initio* software package GAMESS[27] at the restricted Hartree-Fock (RHF) level of theory using the minimal STO-3G[28] basis set.

After a minimum energy structure was identified by the above procedure, this structure was used to initiate a series of molecular mechanics calculations, which using simulated annealing[29] generate several monomer conformations. This procedure involves three steps: heat, run, and cool. The first step was completed using simulation period of heat time (0.1 ps) and a starting temperature of 10 K to set initial velocities with rescaling of velocities at temperature increments of 119 K per 0.01 ps to reach the simulation

temperature of 1200 K. In the second step, the velocities are rescaled at a constant temperature of 1200 K for a run time of 0.5 ps. The final step was the simulation period of cool time (1 ps), with rescaling of velocities at temperature increments of 9 K per 0.01 ps to reach the final temperature of 300 K. The process was repeated until four monomer conformations were obtained from the parent.

Each of these generated conformers was then locally optimized using GAMESS at the RHF/STO-3G level of theory in the same manner as the original 3D structure. The energies of these structures were compared and the structure with the overall minimum energy was then chosen as the "parent" for the next simulated annealing cycle. The lowest energy conformation obtained in the second annealing cycle was used in the simulation of the PDF and NMR spectra. Molecular images were generated using Mercury.[30]

Calculation of ^{13}C Chemical Shielding: The NMR calculations were done using the density functional theory approach with the PBE1PBE[31] exchange correlation functional and using the 4-31G basis set[32] as implemented in Gaussian09 suite of programs[33]. The calculated chemical shielding values were converted to chemical shifts on the tetramethylsilane (TMS) scale using the shielding calculation of methane at the same level of theory, 200.5 ppm, adjusted by -7 ppm which is the chemical shift of dilute methane on TMS scale.[34] Gaussian broadening of 2 ppm along with Lorentzian broadening of 1 ppm was applied on the aliphatic region, with 5 ppm Gaussian broadening used in the aromatic region to obtain the simulated SSNMR spectrum.

Calculation of Atomic PDF: The PDF plots were calculated using DISCUS and plotted using KUPLOT, both part of the DIFFUSE[35] suite of packages. Atomic coordinates of the model were used to calculate a PDF using the following equation

$$G(r) = \frac{1}{r}\sum_{v}\sum_{\mu}\frac{f(0)_v f(0)_\mu}{\langle f(0)\rangle^2}\delta(r - r_{v\mu}) - 4\pi r\rho_o \qquad (1)$$

where r is the radius, δ is the Dirac delta function, ρ_o is the average number density of the kerogen , $f(0)_{\nu}$ and $f(0)_{\mu}$ are the x-ray atomic form factors for atoms ν and μ while $<f(0)>^2$ is the square of the average x-ray atomic form factors. The sum goes over all pairs of atoms ν and μ within the model separated by $r_{\nu\mu}$. The subtraction of $4\pi r\rho_o$ from the G(r) in the above equation leads to the function being equal to zero at large radial distances. While this equation applies for infinite materials with homogenous density confined within well-defined boundaries, kerogen models are finite with irregular shapes and cannot be bound in any way to avoid void space within the boundaries. This leads to a lower average density for the bound model which presents a problem when calculating the pair distribution function using the above equation. To correct for this effect, a modified term is used to describe the shape and size of the kerogen model. The modified equation that allows adjustments for model shape and size, can be derived from Eq. 4 in the paper of Neder and Korsunskiy,[36] is as follows:

$$G(r) = \frac{1}{r}\sum_{v}\sum_{\mu}\frac{f(0)_v f(0)_\mu}{\langle f(0)\rangle^2}\delta(r - r_{v\mu}) - 4\pi r\rho_o \tanh(S(R-r)) \qquad (2)$$

where S is related to the model shape and R the model diameter.

Sample Details: As mentioned in the introduction, experimental data was obtained on a kerogen extracted from a segment of a Green River basin shale core.[24] An elemental

analysis of the kerogen sample used gave an approximately 5% mineral matter content and a dry ash free atomic composition of $C_{100}H_{150}N_3O_8S_1$ for the organic content. This can be compared to the atomic composition of the Siskin model ($C_{645}H_{1017}N_{19}O_{17}S_4$); the only large difference is that the kerogen sample used has a higher oxygen content.

Measurement of Atomic PDF: Measurement of the atomic pair distribution function for a powdered (100 mesh) demineralized Green River kerogen sample[24] was made on instrument 11-ID-B at the Advanced Photon Source (APS), Argonne National Laboratory. High-energy X-rays (60 KeV, λ=0.2128Å) were used with a Perkin Elmer amorphous silicon based detector[38] to collect diffraction data to high values of momentum transfer, Q (Qmax~18Å^{-1}; $Q=4\pi Sin\theta/\lambda$). The 2D diffraction images were processed in Fit2D[37] software to perform x-ray polarization correction and radial integration for peak intensity. Extraction of the experimental pair distribution function from these data was made with PDFgetX2.[39] This software applies corrections to the scattering data for oblique incidence of the x-rays on the image plate, background subtraction, and Compton scattering to produce a structure function, S(Q). The reduced pair distribution function, F(Q) [F(Q)=Q(S(Q)-1)] is Sine-Fourier transformed to yield the atomic pair distribution function, G(r):

$$G(r) = \frac{1}{2\pi}\int_0^\infty Q[S(Q)-1]Sin(Qr)dr \qquad (3)$$

where the transform is truncated at Qmax=18 Å^{-1} due to experimental limitations. The resulting experimental G(r) function yields information on the average bond distances in the kerogen material and can be compared to calculated PDF of kerogen models. Previously, this approach was shown to provide a reasonable comparison and validation of a coal model.[40]

Measurement of ^{13}C solid state NMR: The ^{13}C spectrum of the same Green River kerogen sample used in the PDF measurement was obtained on a Varian Direct Drive (Oversampled) NMR spectrometer operating at a carbon frequency of 25.152 MHz and a proton frequency of 100.02 MHz. The probe was a Chemagnetics 7.5 mm with a ceramic housing for reduced carbon background. The spinning speed was set at 4100 Hz. The pulse delay was 1 s, which is significantly longer than five times the T_1 for the protons. The data was collected using the cross-polarization (CP) method and TPPM[41] decoupling. The contact time was 3 ms which was also more than five times the longest T_{CH} of the aromatic region, as determined from a variable contact time fit[42] of the data. Within the signal to noise ratio differences, the CP spectrum was essentially identical to a single pulse (SP) spectrum. No line broadening was used in this CP spectrum and a total of 146,200 scans were taken.

Results and Discussion

3D Modeling: Our work began with the assumption that the Siskin 2D model of the Green River oil shale kerogen was the most complete and reliable structural model that is presently available (Figure 1). This structure was incorporated into the molecular modeling scheme using the general procedure described above. The initial starting point was the 3D structure designated as S1 in Figure 2; this represents the starting point for the folded structure which was used to begin the search for lower local energy minima structures. The RHF single point energy of this local structure is −28569.2846 Hartree (1 Hartree = 627.509 kcal/mol).

Following the annealing/optimization process described above using the S1 structure, four additional low energy structures, shown in Figure 3, were identified: S2 (E_{RHF} = −28569.7319 Hartree), S3 (E_{RHF} = −28569.6691 Hartree), S4 (E_{RHF} = −28570.3721 Hartree), and S5 (E_{RHF} = −28569.9504 Hartree). The lowest energy of these initial five structures, S4, was then used as the parent for another annealing/optimization cycle, generating structures S4-1 through S4-5. These structures are shown in Figure 4. These ten structures were all optimized at the RHF level to relax the geometries obtained from the MM+ calculations. It should be noted that due to the size of these systems, it is not feasible to obtain a completely optimized structure. The initial and final RHF energies are listed in Table 1. This shows that the structures obtained from MM+ are, on the average, 1 Hartree higher than those calculated from RHF. The lowest energy structure after the optimization is S4-5 (E_{RHF} = -28571.4952 Hartree). This S4-5 structure was the one used to obtain the simulations of ^{13}C NMR and PDF measurements, used to validate the model.

NMR: In order to explore the sensitivity of the simulated ^{13}C NMR spectrum to the structure of the model, calculations of the chemical shielding were completed on structures S4-1 through S4-5 and these calculations were used to simulate the spectra shown in Figure 5. As can be seen in this figure, the spectra obtained by from any of these models are very similar, with only slight differences in the aliphatic chemical shift region. This is not unexpected, as nearly all the structural changes in the models are occurring in the flexible aliphatic chains while the aromatic structures are very rigid and fixed.

A comparison between the spectrum simulated for model S4-5 and an experimental ^{13}C SSNMR spectrum of a Green River kerogen is shown in Figure 6. The agreement between the simulation and the experimental spectrum is quite good in terms of the agreement of the line shape for both the aliphatic and aromatic regions as well as in the relative intensities of the two regions. The agreement of the relative intensities is a reflection that the model accurately reflects the experimentally observed ratio between aromatic and aliphatic carbons (28% aromatic/olefinic/carbonyl for the model and 24% from the experimental NMR). The similarity in the lineshapes, is an indication that the distribution of carbon types in also being accurately reproduced in the model. For instance, both the experimental and the simulated spectra show the same tail to higher chemical shifts, due to the presence of the carbonyl carbons.

PDF: A similar analysis was completed with the atomic pairwise distribution functions in order to obtain a second independent validation of the model. The PDF simulated based on the S4-5 monomer model is shown in Figure 7, along with the decomposition to the pairings between different atom types. The plot shows that the atom-atom correlations are consistent with the separations expected based on typical carbon bond lengths and angles: C–H (1.12 Å), C–C (1.52 Å), ∠ C–C–H (2.18 Å), ∠ C–C–C (2.56 Å), and dihedral C–C–C–C (3.90 Å). The features above 3 Å are a function of the 3D structure and should show sensitivity to changes in the model. A comparison of the PDFs of the structures S4-1 to S4-5 is shown in Figure 8. The plots do not show any significant deviation from each other which indicates that in general the average of various geometrical parameters such as bond lengths, bond angles, and torsional angles are the same for all structures.

To gauge the sensitivity of the PDF analysis to the structural model a stoichiometric equivalent 2D model of the kerogen Siskin model but using only aliphatic groups was built and its PDF was generated. As shown in Figure 8, the PDF of the aliphatic model is clearly different from the PDF obtained from the other models in the region above 3 Å. Hence, the PDF approach provides unique plots for different chemical structures and can be used for our analysis.

The ultimate test, of course, is how well the PDF of the models correlate with the experimental PDF. A preliminary comparison of the model and experimental PDFs suggested that both have the same features in the short range region ($r < 3$ Å) but deviates heavily at longer distances. There are two possible reasons for this discrepancy: (1) the model is considerably smaller than the experimental structure and (2) a correction term as discussed in the experimental section which accounts for the shape and size of the model is necessary for comparison with experiment.

To explore the effect of the size of the model, a much larger model was built by confining twelve of the unoptimized Siskin model structures (S1) in a bounding box just large enough to accommodate the model. This last point is crucial as the correction term mentioned in point two above, assume a totally filled rectangular box with no void spaces.

The PDF of the 12-unit kerogen model and the experimental PDF for the Green River kerogen are shown in Figure 10. The PDF of the model is corrected accordingly for size and shape. The first peak in the PDFs corresponds to C-H distances whereas the second corresponds to the C-C distance between directly bonded carbons. This distance is approximately 1.5 Å for aliphatic carbons and 1.4 Å for aromatic ones. The second peak at approximately at 2.5 Å corresponds to the geminal distance between carbons two bonds apart. This distance is approximately 2.4 Å and 2.6 Å for aromatic and aliphatic carbons, respectively. The peak at approximately 3 Å corresponds to the distance between carbons separated by four bonds in a *cis* configuration and the one at approximately 3.8 Å to carbons in a *trans* configuration. For these peaks good agreement in terms of peak position and intensity is observed. ANYTHING ELSE HERE?

Conclusion

Several 3D models based on Siskin's 2D model for a Green River kerogen were constructed by the geometry optimization of different conformations provided by simulated annealing techniques. These models were used to obtain simulated PDF plots and ^{13}C NMR spectra which were compared with experimental data obtained on a Green River kerogen sample. This process allowed for the exploration of both the sensitivity of these experimental methods to the 3D structure as well as for the validation of the use of the models for subsequent modeling work.

Using different single unit models, simulations of the expected ^{13}C NMR spectrum were completed. These simulated spectra are all similar, but do show differences in the line shape in the aliphatic region. The comparison between the experimental and simulated spectra is quite good, in terms of the lineshapes of both the aromatic and aliphatic region as well as in the relative signal intensity between the two peaks.

The initial models consisting of a single kerogen unit were not sufficient to mimic the bulk kerogen as can be seen in their respective PDF plots. A larger 12-unit model

was therefore constructed in a manner which minimized the amount of "dead" spaces around the corners of our confining box, as the calculation of the PDF is based on a rectangular box with no void spaces around the molecule. Overall there is good agreement between the model and experimental PDF plots especially at shorter distances, however less accurate for distances between 4 Å and 6 Å. For distances above 6 Å the PDF provides very poor resolution and while there is overall agreement between the model and experimental one, this does not provide any apparent structural information.

Acknowledgments: This work is supported by a grant from the U.S. Department of Energy, National Energy Technology Laboratory. Use of the Advanced Photon Source was supported by the U. S. Department of Energy, Office of Science, Office of Basic Energy Sciences, under Contract No. DE-AC02-06CH11357. An allocation of computer time from the Center for High Performance Computing at the University of Utah is acknowledged. A. M. O. acknowledges beam time awards on 11-ID-B and 12-ID-B at the Advanced Photon Source at Argonne National Laboratory. D.R.L. acknowledges support by the Chevron Energy Technology Company through a contract with University of Utah.

References

(1) Behar, F.; Vandenbroucke M. *Revue De L'Institut Francais Du Petrole* **1986**, *41*, 173.
(2) Rullkötter, J.; Michaelis, W. *Org Geochem* **1990**, *16*, 829.
(3) Siskin, M.; Katritksy, A. In *Composition, Geochemistry and Conversion of Oil Shales*, NATO ASO Series, Series C: Mathematical and Physical Sciences-Vol. 455, C. Snape, ed., Kluwer Academic Publishers, Dordrecht/Boston/London, **1995**, p. 313.

(4) Nomura, M.; Artok, L.; Murata, S.; Yamamoto, A.; Hama, A.; Gao, H.; Kidena, K. *Energy Fuels* **1998**, *12*, 512.
(5) van Krevelen, D.W. *Coal: Typology – Chemistry – Physics – Constitution*. Netherlands: Elsevier; **1961**.
(6) Brons, G.; Siskin, M.; Botto, R.I.; Guven, N. *Energy Fuels* **1989**, *3*, 85.
(7) Siskin, M.; Katritzky, A.R. *Science*. Washington, DC; **1991**, *254*, 231.
(8) Smith, J.W.; Higby, L.W. *Anal. Chem.* **1960**, *32*, 17.
(9) Reisberg, J. *Prepr. Pap. – Am. Chem. Soc., Div. Fuel Chem*. **1980**, *25*, 116.
(10) Reisberg, J. In: Stauffer, H.C., editor. *Oil Shale, Tar Sands, and Related Materials*. ACS Symposium Series 163; American Chemical Society, Washington, DC; **1981**, p. 155.
(11) Vanderbroucke, M. Oil & Gas Science and Technology-Rev. IFP, **2003**, *58* (2), 243.
(12) Durand, B; Vanderbroucke, M. As cited in *Kerogen, Insoluble Organic Matter From Rocks*, B. Durand, ed., Technip, **1980**, p. 218 and 319.

(13) Siskin, M.; Scouten, C.G.; Rose, K.D.; Aczel, D.; Colgrove, S.G.; Pabst, R.E. In: Snape, C., editor. *Composition, geochemistry and conversion of oil shales*. Netherlands: Kluwer Academic; **1995**, p. 143.
(14) Lille, U.; Heinmaa, I.; Pehk, T. *Fuel* **2003**, *82*, 799.
(15) Faulon, J.L.; Vandernbroucke, M.; Drappier, J.M.; Behar, F.; Romero, M. *Organic Geochemistry*, **1990**, *6*, 981; Faulon, J.L. *Prediction, elucidation et modelisation moleculaire: algorithms et applications*. **1991,** Ph. D. Thesis.

(16) Freund, H.; Walters, C.C.; Kelemen, S.R.; Siskin, M.; Gorbaty, M.L.; Curry, D.J.; Bence, A.E. *Org. Geochem.* **2007**, *38*, 288.
(17) Vandergrift, G.F.; Winans, R.E.; Horwitz, E.P. *Fuel* **1980**, *59*, 634.
(18) Jeong, K.M.; Patzer II, J.F. *Indigenous Mineral Matter Effects in Pyrolysis of Green River Oil Shale*, In Geochemistry and Chemistry of Oil Shales, American Chemical Society, **1983**, p. 529.
(19) Jeong K.M.; Kobylinski, T.P. *Organic-Mineral Matter Interactions in Green River Oil Shale*, American Chemical Society, **1983**, p. 493.
(20) Sheu, E.Y. *Self-Association of Asphaltenes; Structure and Molecular Packing*, In: Mullins, O.C.; Sheu, E.Y., editors. Structure and Dynamics of Asphaltenes, Plenum Press, New York, **1998**, p.115.
(21) Egami, T.; Billinge, S.J.L. *Underneath the Bragg Peaks: Structure Analysis of Complex Materials*; Oxford/Pergamon Press, New York, **2004**.
(22) Nield, V.; Keen, D.A.; *Diffuse Neutron Scattering from Crystalline Materials*; Oxford/Clarendon Press, Oxford, **2001**.
(23) Solum, M.S.; Pugmire, R.J.; Grant, D.M. *Energy & Fuels*, **1989**, *3*, 187-193.
(24) Solid state ^{13}C NMR and PDF measurements were completed on a sample of kerogen isolated following the process outlined by Vandergrift, G. F.; Winans, R. E.; Scott, R. G.; Horwitz, E. P., in Fuel 1980, 59(9), 627, on a one foot section from the peak organic content of the Mahogany zone of a core drilled in the Green River Formation of the Uinta Basin in Utah in spring 2010. The experimental results will be discussed further in a separate publication.
(25) HyperChem(TM) Professional 7, Hypercube, Inc., 1115 NW 4th Street, Gainesville, Florida 32601, USA.
(26) Allinger, N.L. *J. Am. Chem. Soc.*, **1977**, *99*, 8127.
(27) Schmidt, M.W.; Baldridge, K.K.; Boatz,J.A.; Elbert, S.T.; Gordon, M.S.; Jensen, J.J.; Koseki, S.; Matsunaga, N.; Nguyen, K.A.; Su, S.; Windus, T.L.; Dupuis, M.; Montgomery, J.A. *J.Comput.Chem.*, **1993**, *14*, 1347.
(28) Hehre, W.J.; Stewart, R.F.; Pople, J.A. *J. Chem. Phys.* **1969**, *51*, 2657.
(29) Kirkpatrick, S.; Gelatt, C.D.; Vecchi, M.P. *Science* **1983**, *220*, 671.
(30) Macrae, C.F.; Bruno, I.J.; Chisholm, J.A.; Edgington, P.R.; McCabe, P.; Pidcock, E.; Rodriguez-Monge, L.; Taylor, R.; van de Streek, J.; Wood, P.A. *J. Appl. Cryst*. **2008**, *41*, 466.
(31) Adamo, C; Barone, V., *J. Chem. Phys.*, **1999**, *110*, 6158-69.
(32) Ditchfield, R.; Hehre, W.J.; Pople, J.A. *J. Chem. Phys.*, **1971**, *54*, 724; Hehre, W.J.; Ditchfield, R.; Pople, J.A. *J. Chem. Phys.*, **1972**, *56*, 724.
(33) Gaussian 09, Revision B.01, Frisch, M. J.; Trucks, G. W.; Schlegel, H. B.; Scuseria, G. E.; Robb, M. A.; Cheeseman, J. R.; Scalmani, G.; Barone, V.; Mennucci, B.; Petersson, G. A.; Nakatsuji, H.; Caricato, M.; Li, X.; Hratchian, H. P.; Izmaylov, A. F.; Bloino, J.; Zheng, G.; Sonnenberg, J. L.; Hada, M.; Ehara, M.; Toyota, K.; Fukuda, R.; Hasegawa, J.; Ishida, M.; Nakajima, T.; Honda, Y.; Kitao, O.; Nakai, H.; Vreven, T.; Montgomery, Jr., J. A.; Peralta, J. E.; Ogliaro, F.; Bearpark, M.; Heyd, J. J.; Brothers, E.; Kudin, K. N.; Staroverov, V. N.; Kobayashi, R.; Normand, J.; Raghavachari, K.; Rendell, A.; Burant, J. C.; Iyengar, S. S.; Tomasi, J.; Cossi, M.; Rega, N.; Millam, N. J.; Klene, M.; Knox, J. E.; Cross, J. B.; Bakken, V.; Adamo, C.; Jaramillo, J.; Gomperts, R.; Stratmann, R. E.; Yazyev, O.; Austin, A. J.; Cammi, R.; Pomelli, C.; Ochterski, J. W.;

Martin, R. L.; Morokuma, K.; Zakrzewski, V. G.; Voth, G. A.; Salvador, P.; Dannenberg, J. J.; Dapprich, S.; Daniels, A. D.; Farkas, Ö.; Foresman, J. B.; Ortiz, J. V.; Cioslowski, J.; Fox, D. J. Gaussian, Inc., Wallingford CT, 2009.
(34) Jameson, A.K.; Jameson, C.J. *Chem. Phys. Lett.* 1987, *134*, 461.
(35) Proffen, T.; Neder, R.B. *J. Appl. Crystallogr.* **1997**, *30*, 171.
(36) Neder, R.B.; Korsunskiy, V.I. *J. Phys.: Condens. Matter*, **2005**, *17*, S125.
(37) Hammersley, A.P.; Svensson, S. O.; Hanfland, M.; Fitch, A.N.; Hausermann, D. *High Pressure Research*, **1996**, *14*, 235.
(38) Chupas, P. J.; Chapman, K. W.; Lee, P. L. *J. Appl. Cryst.*, **2007**, *40*, 463.
(39) Qiu, X.; Thompson, J.W.; Billinge, S.J.L. *J. Appl. Cryst.*, **2004**, *37*, 678.
(40) Winans, R.E.; Chapman, K.W.; Chupas, P.J.; Seifert, S.; Clemens, A.H.; Calo, J.; Bain, E.; Mathews, J.P.; Narkiewicz, M.R. *Prep. Pap. - Am. Chem. Soc., Div Fuel Chem.*, **2008**, *53(1)*, 283.
(41) Bennett, A. E., Rienstra, C. M., Auger, M., Lakshmi, K. V., Griffin, R. G.; *J. Chem. Phys.,* 103, **1995**, 6951.
(42) Kolodziejski, W., Klinowski, J., *Chem. Rev.*, 102, **2002**, 613.

Table 1: RHF/STO-3G initial and final energies (in Hartree) of the different monomer kerogen models. The S2 to S5 structures were obtained from the simulated annealing procedure on S1. Structures S4-1 through S4-5 were derived from the lowest energy conformer (S4) from the first annealing step.

	Energy (Hartree)	
	Initial Structure	Final Structure
S1	–28569.2846	-28570.5355
S2	–28569.7319	-28570.5929
S3	–28569.6691	-28570.4581
S4	–28570.3721	-28571.1721
S5	–28569.9504	-28570.4481
S4-1	–28569.8771	-28571.4328
S4-2	–28569.8316	-28571.3913
S4-3	–28569.9410	-28571.4887
S4-4	–28569.8622	-28571.4575
S4-5	–28569.9061	-28571.4952

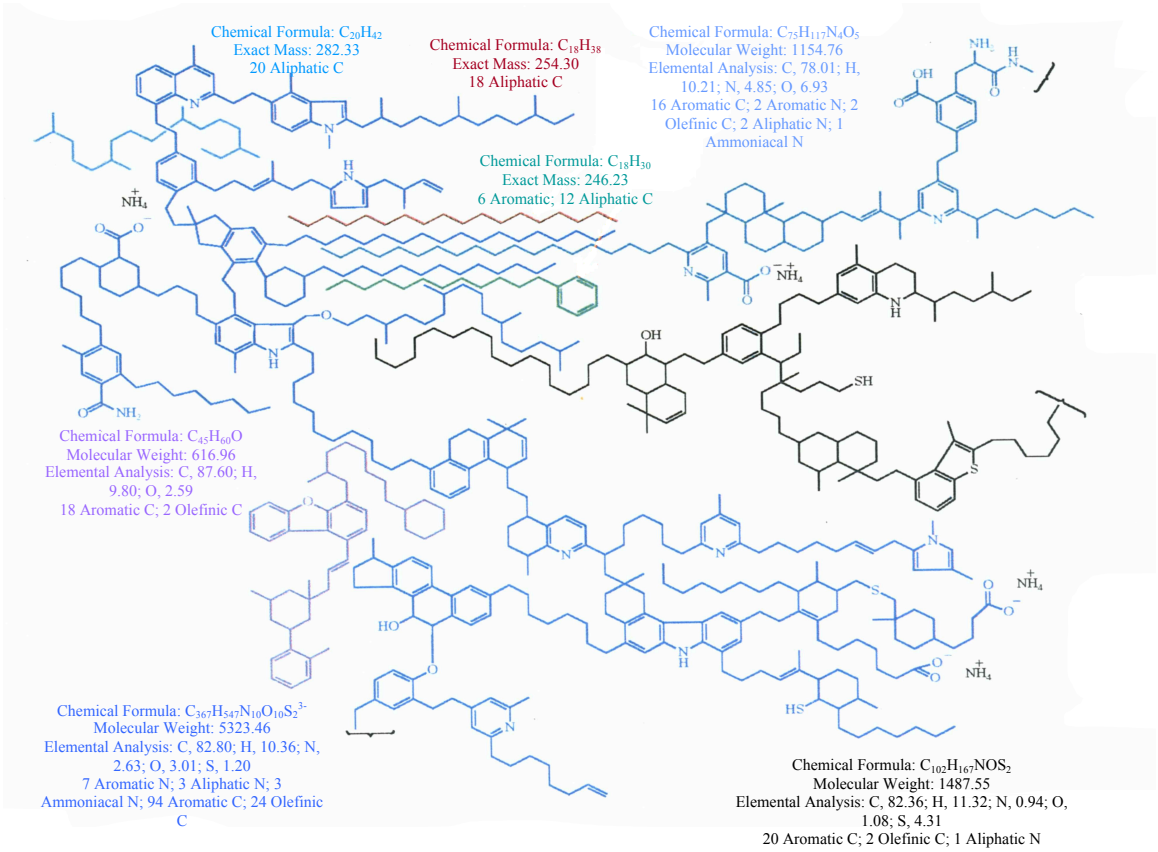

Fig. 1: The 2D Siskin model of Green River kerogen, taken from ref 13.

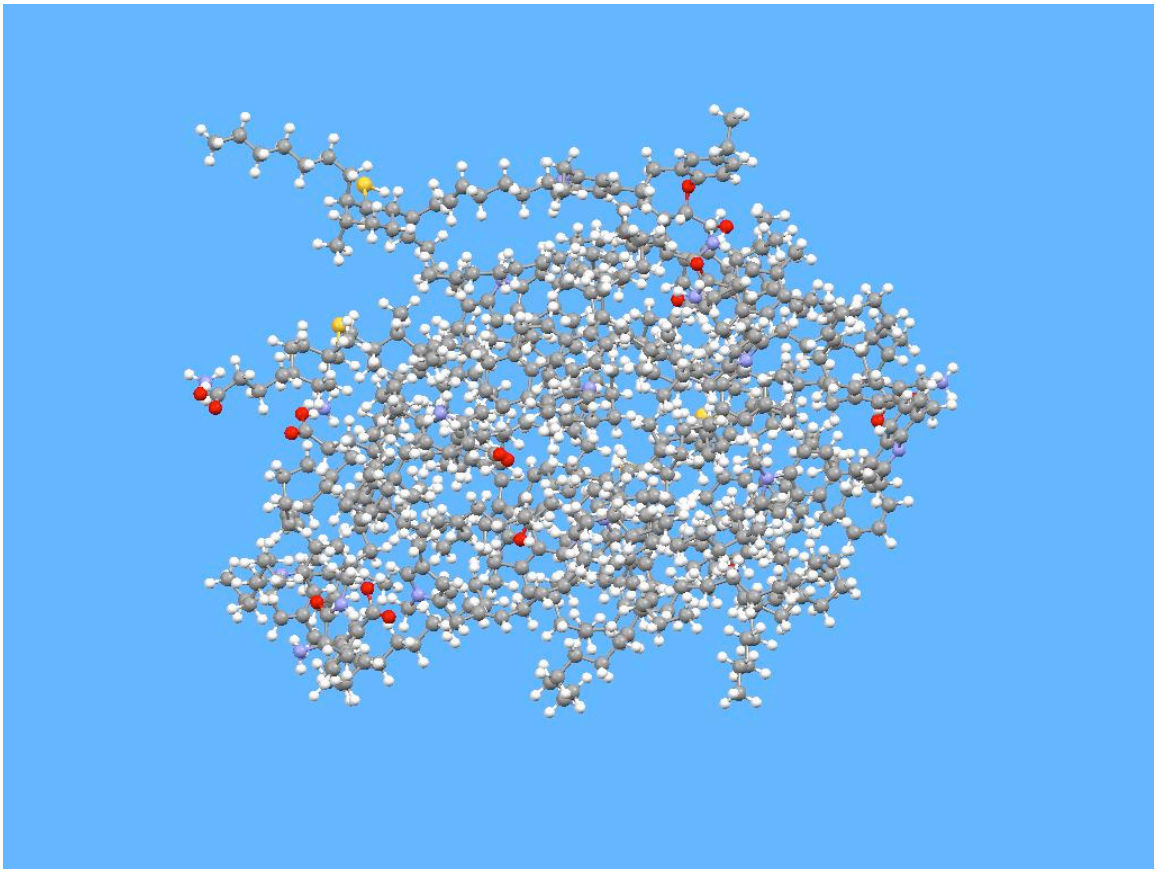

Fig. 2: Initial 3D model (S1) of the Green River kerogen Siskin model (1702 atoms). The atom colors are as follows: C - gray, O - red, N - blue, S - yellow, H - white. The tubes represent the molecule's backbone and the spheres represent the atoms.

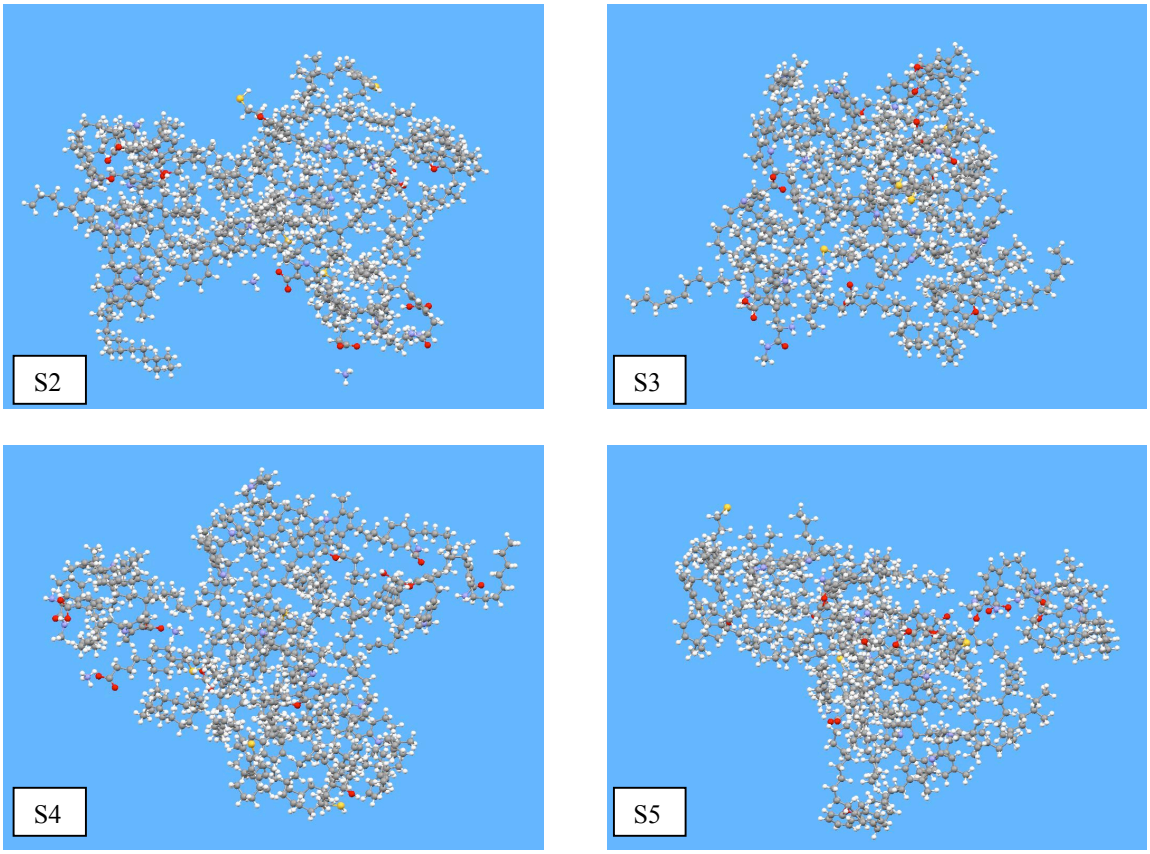

Fig. 3: Local structures generated by applying the simulated annealing procedure described on the initial 3D kerogen model S1. The atom colors and molecule description are the same as in Fig. 2.

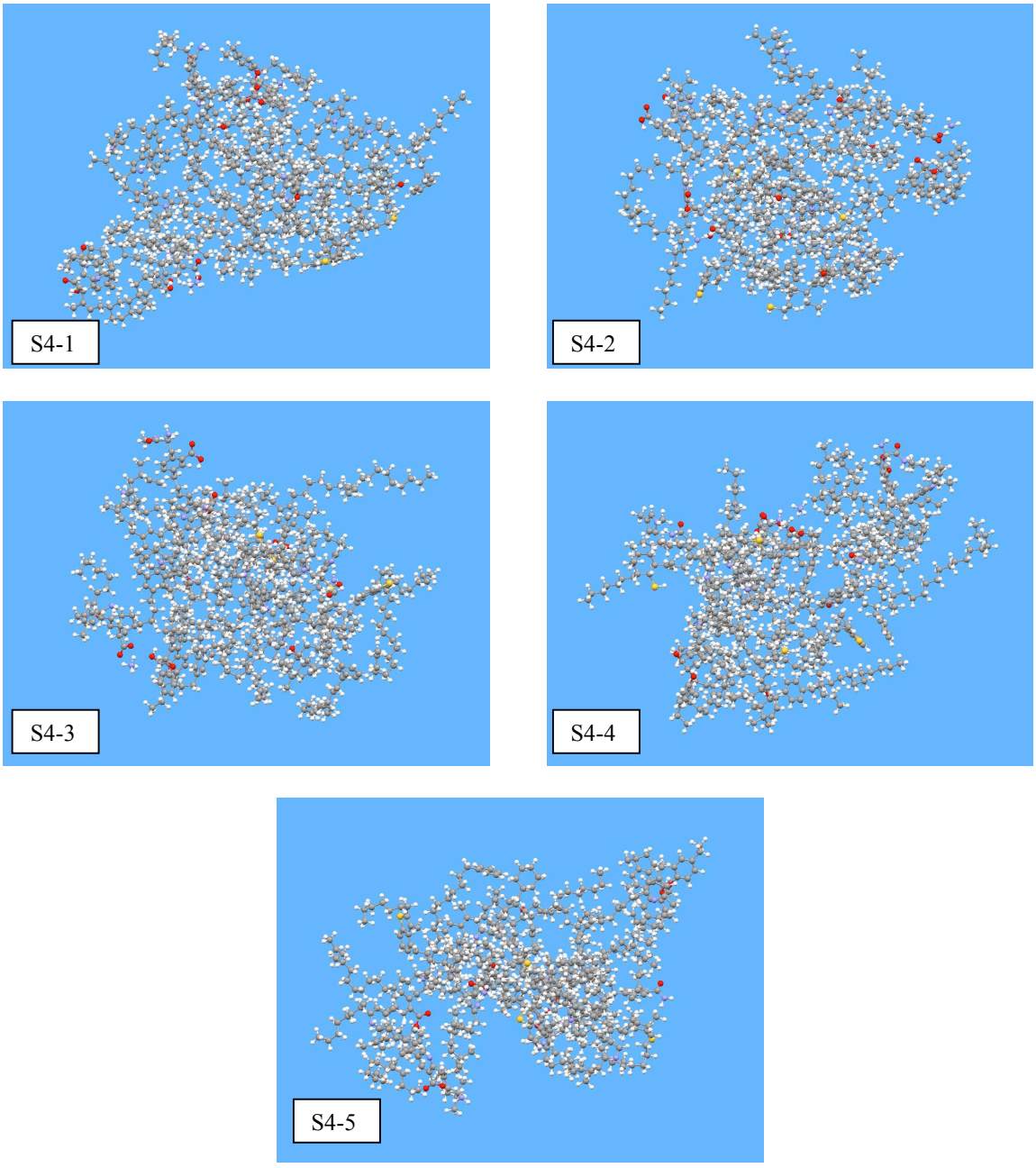

Fig. 4: Local structures generated by subjection kerogen structure S4 to the simulated annealing procedure. The atom colors and molecule description are the same as in Fig. 2.

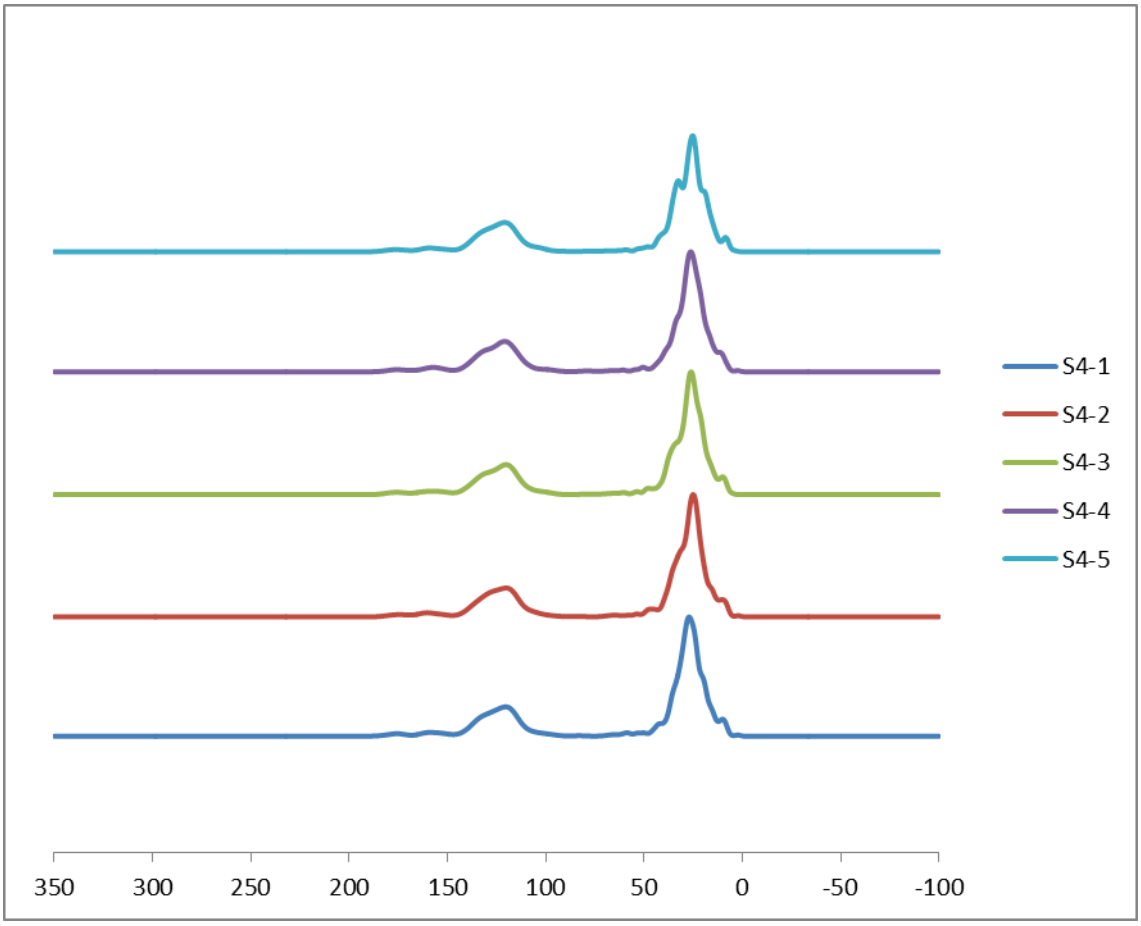

Fig 5: Simulated ^{13}C NMR spectra for models S4-1 thorough S4-5

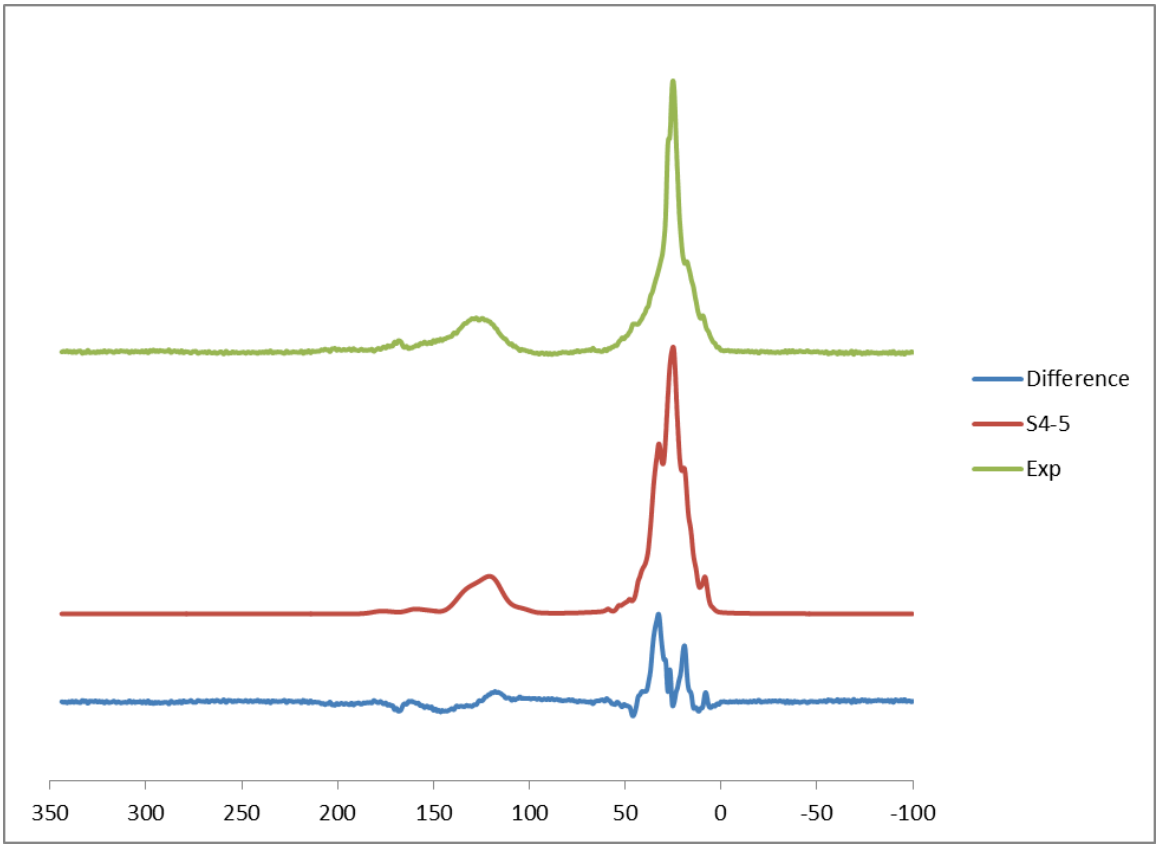

Fig 6: Comparison between simulated ^{13}C NMR spectrum from model S4-5 and the experimental solid state ^{13}C NMR spectrum obtained on a Green River oil shale kerogen. The RMS difference between S4-5 and experimental spectrum is 8 ppm.

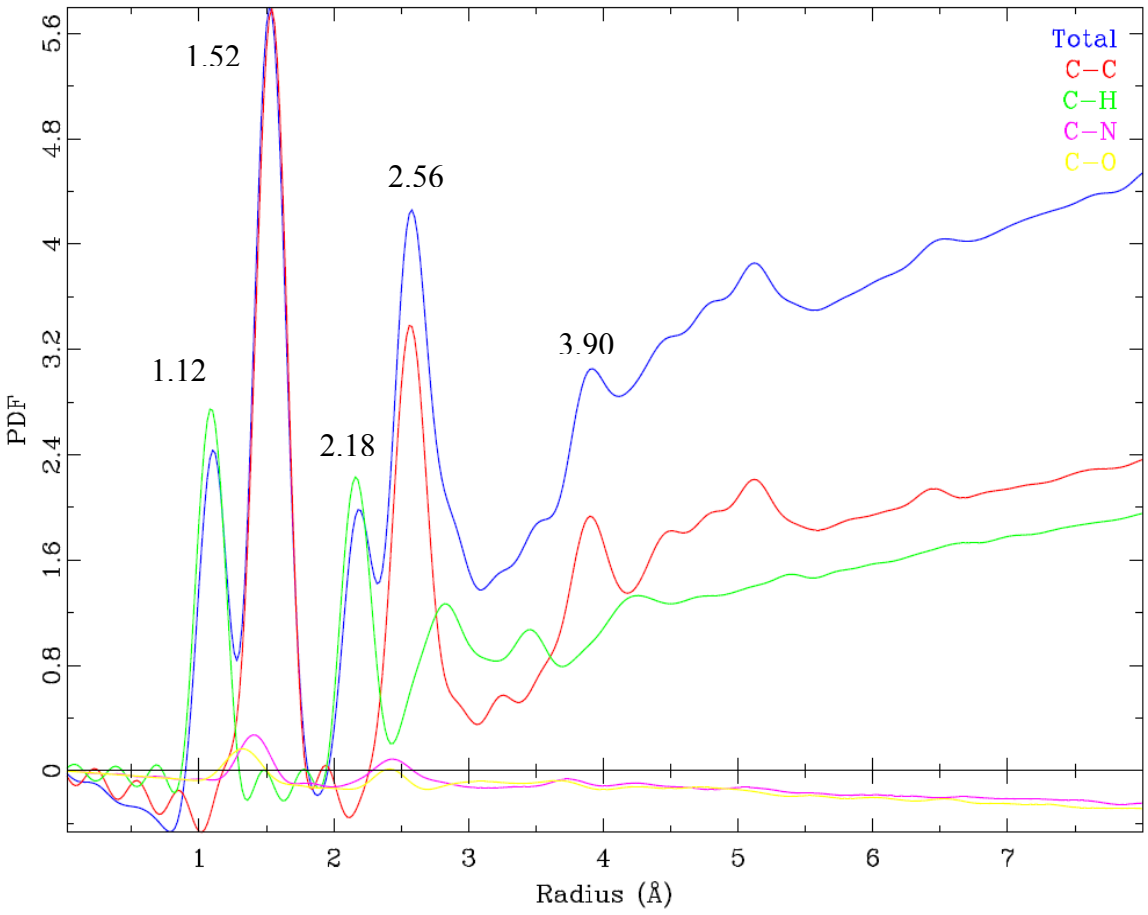

Fig. 7: Pair distribution functions (PDFs) of atom-atom correlations in the kerogen monomer model S4-5. The correlation is decomposed to the contributions from different atomic pairings.

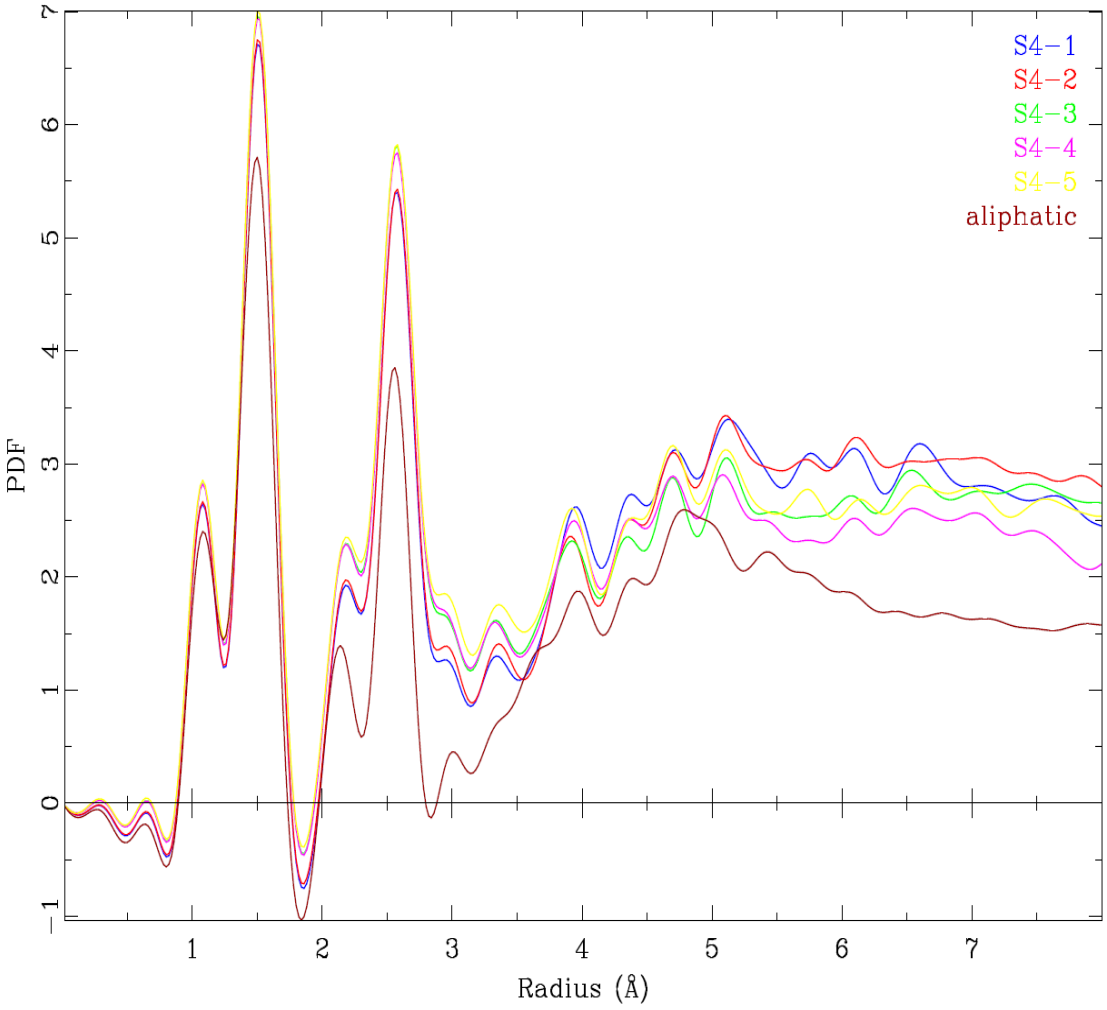

Fig. 8: PDFs of the five monomer conformations of kerogen obtained from the lowest energy structure S4. A stoichiometric equivalent aliphatic structure is included to show that the PDF method is sensitive to varying structures.

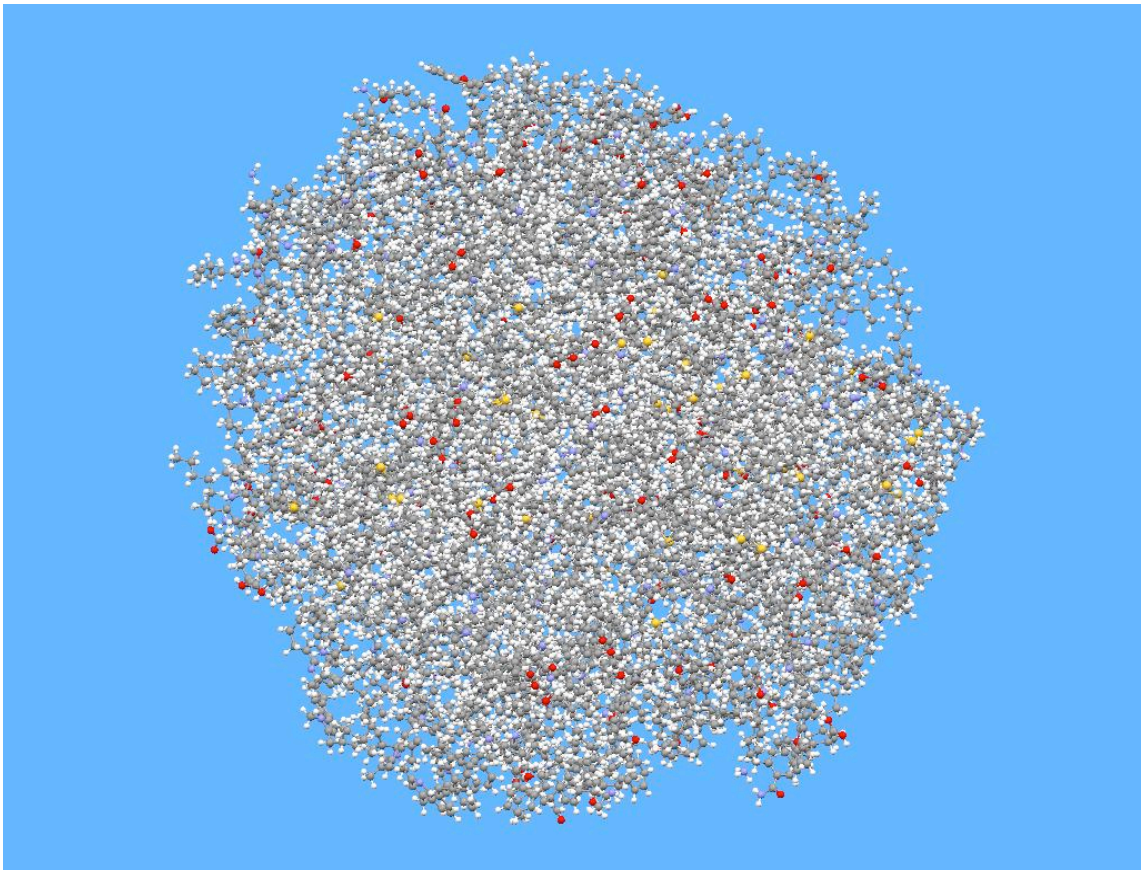

Fig. 9: Three-dimensional structures of the 12-unit kerogen models. The atom colors and molecule description are the same as in Fig. 2.

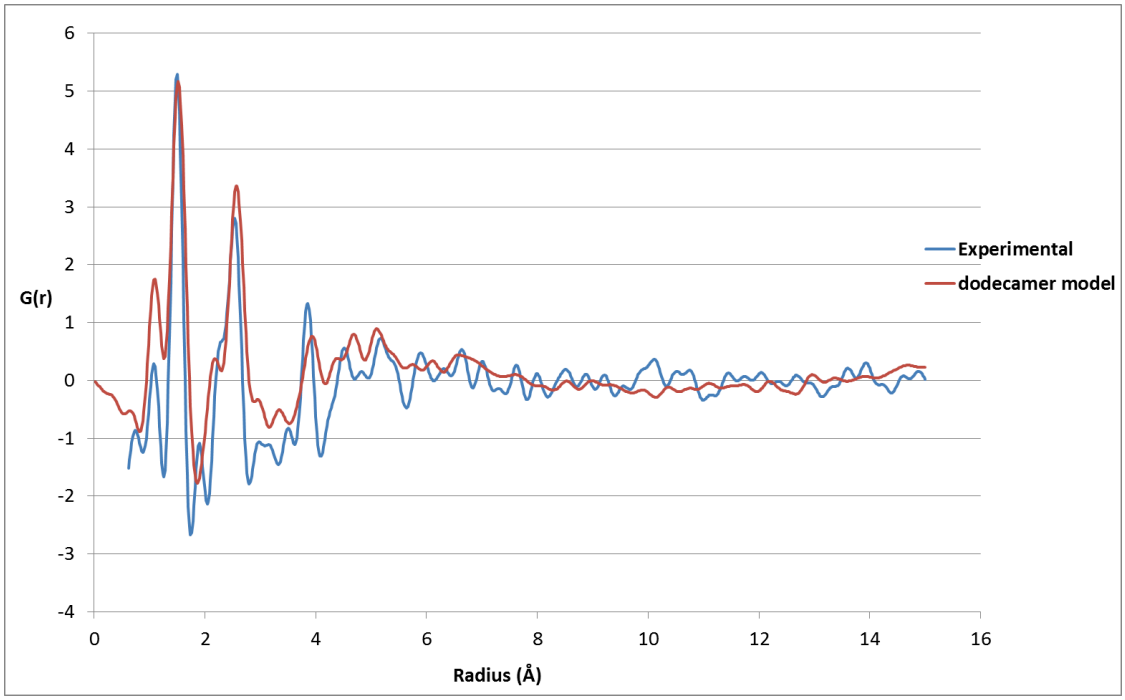

Fig. 10: Comparison of experimentally determined PDF for Green River kerogen and the 12-unit model. The dodecamer model was shape and size corrected using the modified function $-4\pi r\rho_o \tanh(S(R-r))$ with S=0.05 and R=19.3 Å.

First Results and Simulation of AMSO's RD&D Process Tests

Alan K. Burnham et al.
Chief Technology Officer
American Shale Oil, LLC

Presented at:
Unconventional Fuels Conference
Salt Lake City, UT, May 15, 2012

AMSO is one of three RD&D Leaseholders in Colorado's Piceance Basin

- **AMSO LLC is a 50/50 joint venture of Genie Energy Ltd and TOTAL S.A.**
  - Genie is the operating partner during R&D; Total is during commercial operations
  - Genie also has an oil shale venture in Israel (IEI)
  - TOTAL also has other oil shale ventures (e.g., with Red Leaf in Utah)
- **The lease was originally issued to EGL Resources in 2007**
- **Using the USGS 2-million barrels-per-acre estimate, this area contains ~10 billion barrels of potential resource**

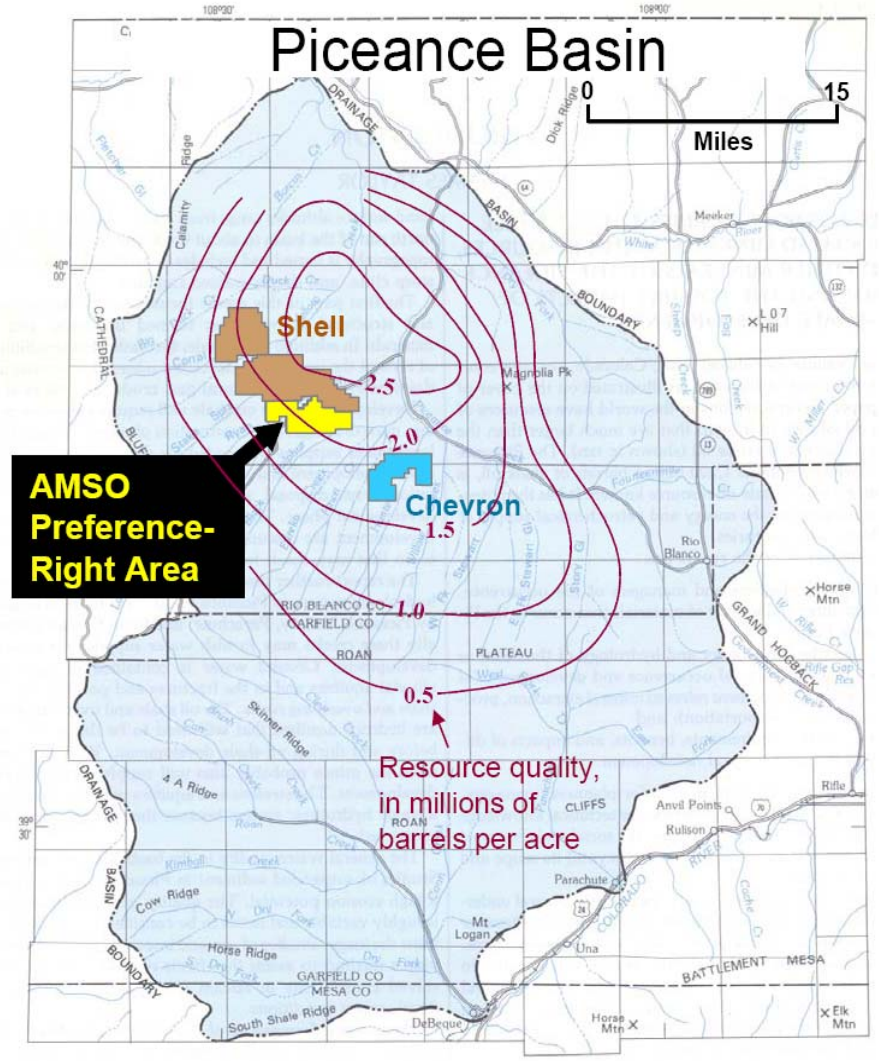

AMSO is initially targeting illite-rich oil shale below the saline zone on its RD&D tract

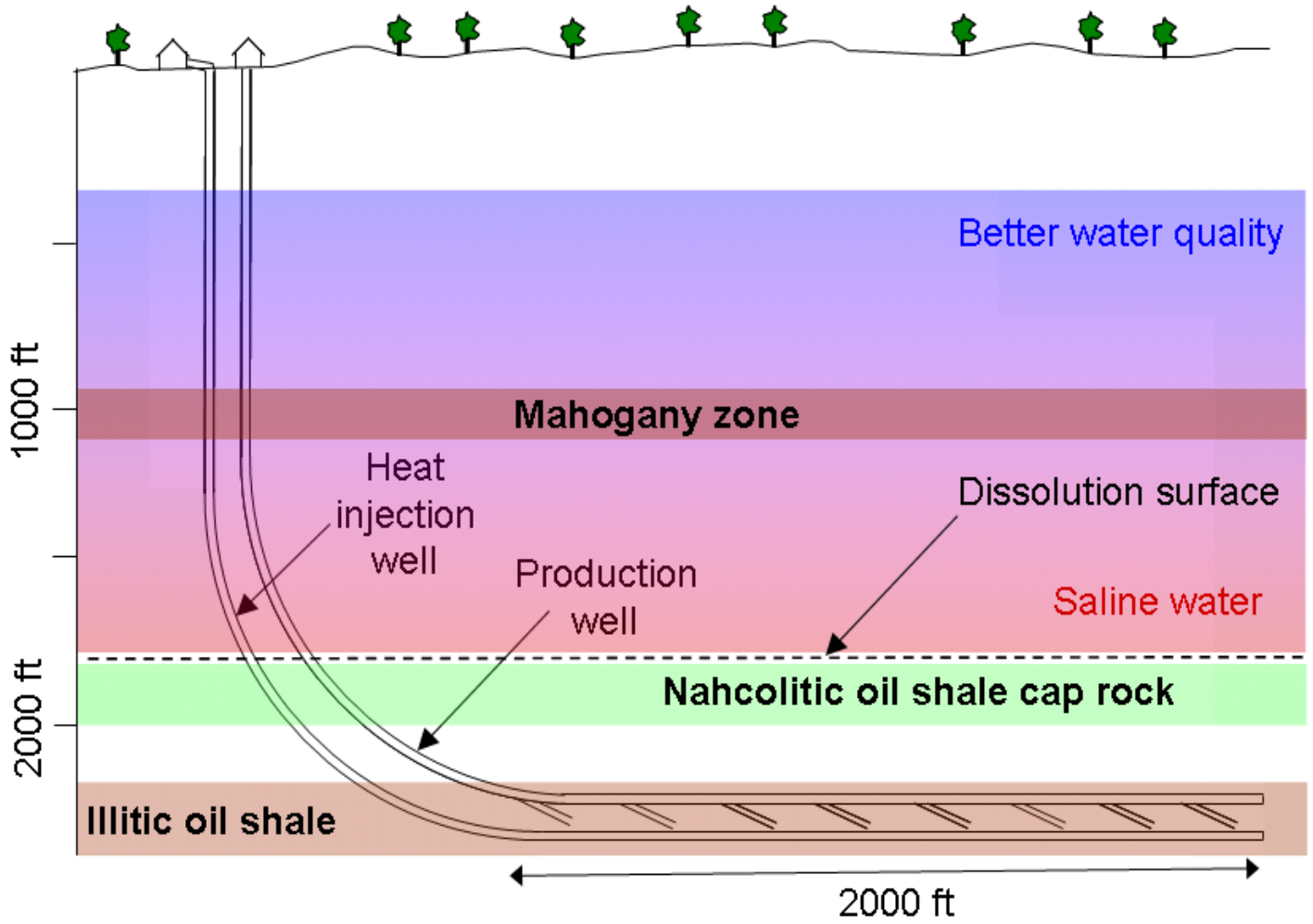

- Minimal surface footprint
- Protection of aquifers
- Low water usage
- High energy efficiency
- Low gas emissions
- High-value jobs

Our RD&D Plan aims to demonstrate important aspects of our process

- **Geochemical and geomechanical properties of the illitic oil shale**
- **Hydrologic isolation of the illitic oil shale from protected waters**
- **Adequate heat transfer using a boiling oil pool**
  - Central to the Conduction, Convection, Reflux (CCR™) concept
  - Enhancement by thermo-mechanical fragmentation
- **Premium oil quality**
  - High API gravity, low metals content, low nitrogen content
- **Minimal water usage (<1 barrel of water per barrel of oil)**
- **Ability to meet all applicable air emission regulations**
- **Technology for carbon sequestration**
- **Economic viability**

The AMSO process uses convective heat transfer via permeability from thermo-mechanical fragmentation

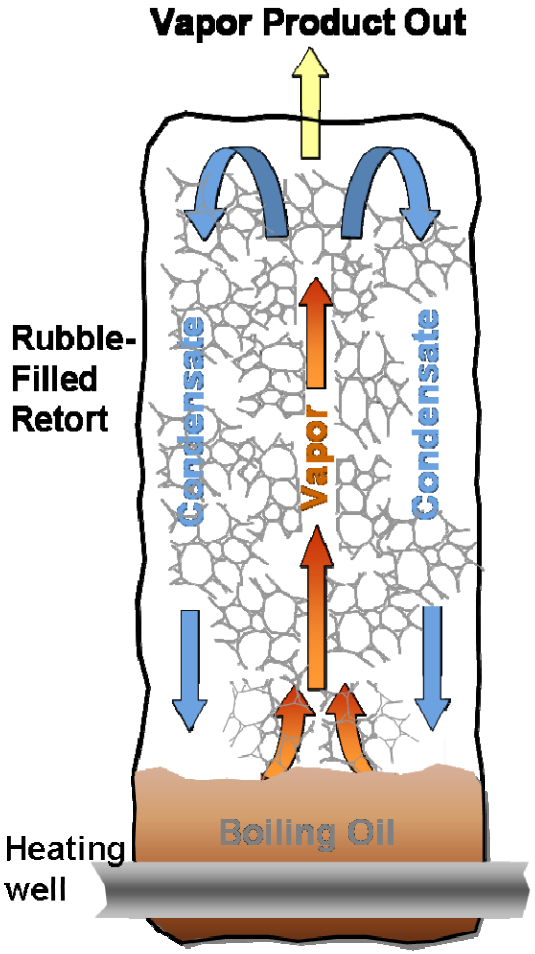

From Prats et al., JPT, 1977

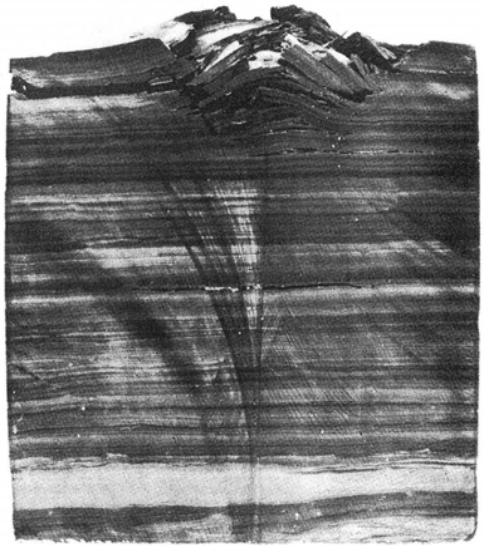

Confined on all but one side

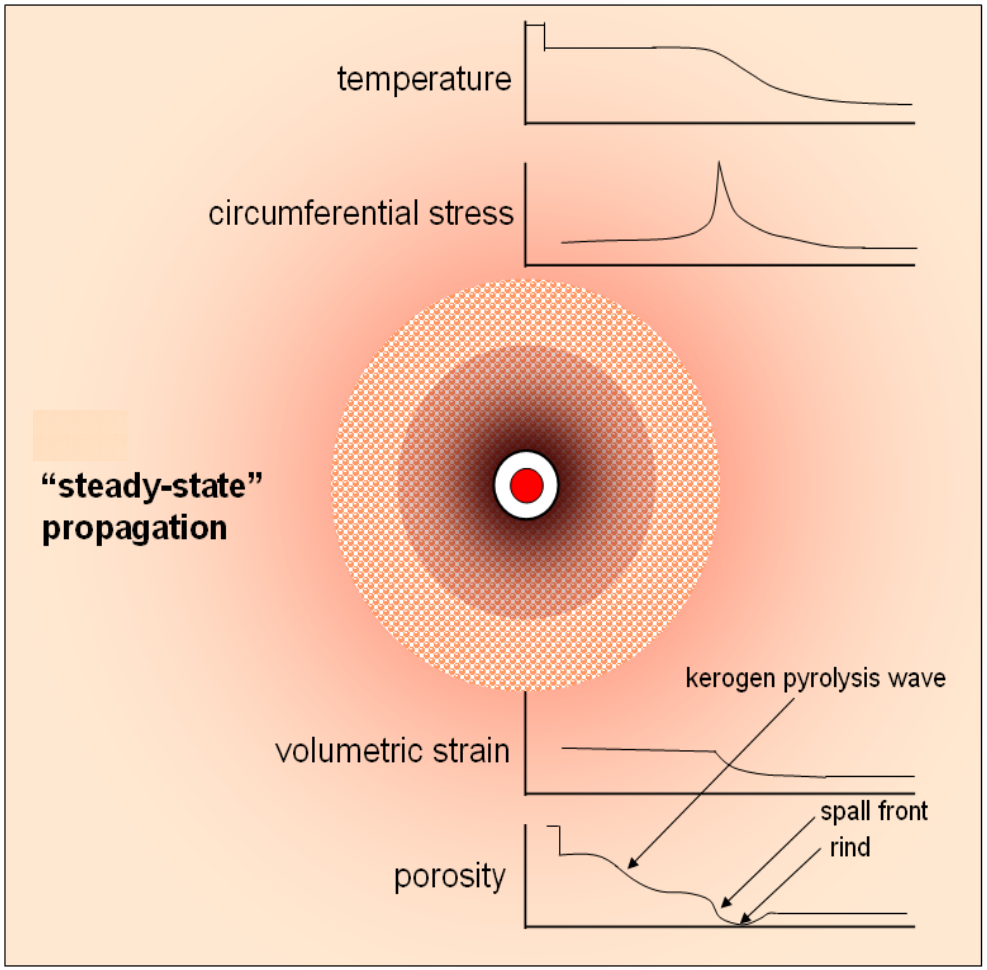

The University of Utah (ICSE*) is developing models to simulate and optimize our process

- Developing rock mechanics models to estimate load-bearing capability, thermal fracture (crack) characteristics, and porosity and permeability
- Modeling the relative importance of conductive and convective heat transfer rates as a function of rubble characteristics
- Simulating heat transfer rates in our pilot test geometry at various levels of approximation
- Developing reservoir simulators capable of modeling the entire range of important chemical and physical processes

*ICSE = Institute for Clean and Secure Energy

Deformation, load bearing capacity, porosity and permeability are required for numerical simulations

- Oil shale changes from elastic to viscoelastic to plastic as temperature increases, so modeling is difficult

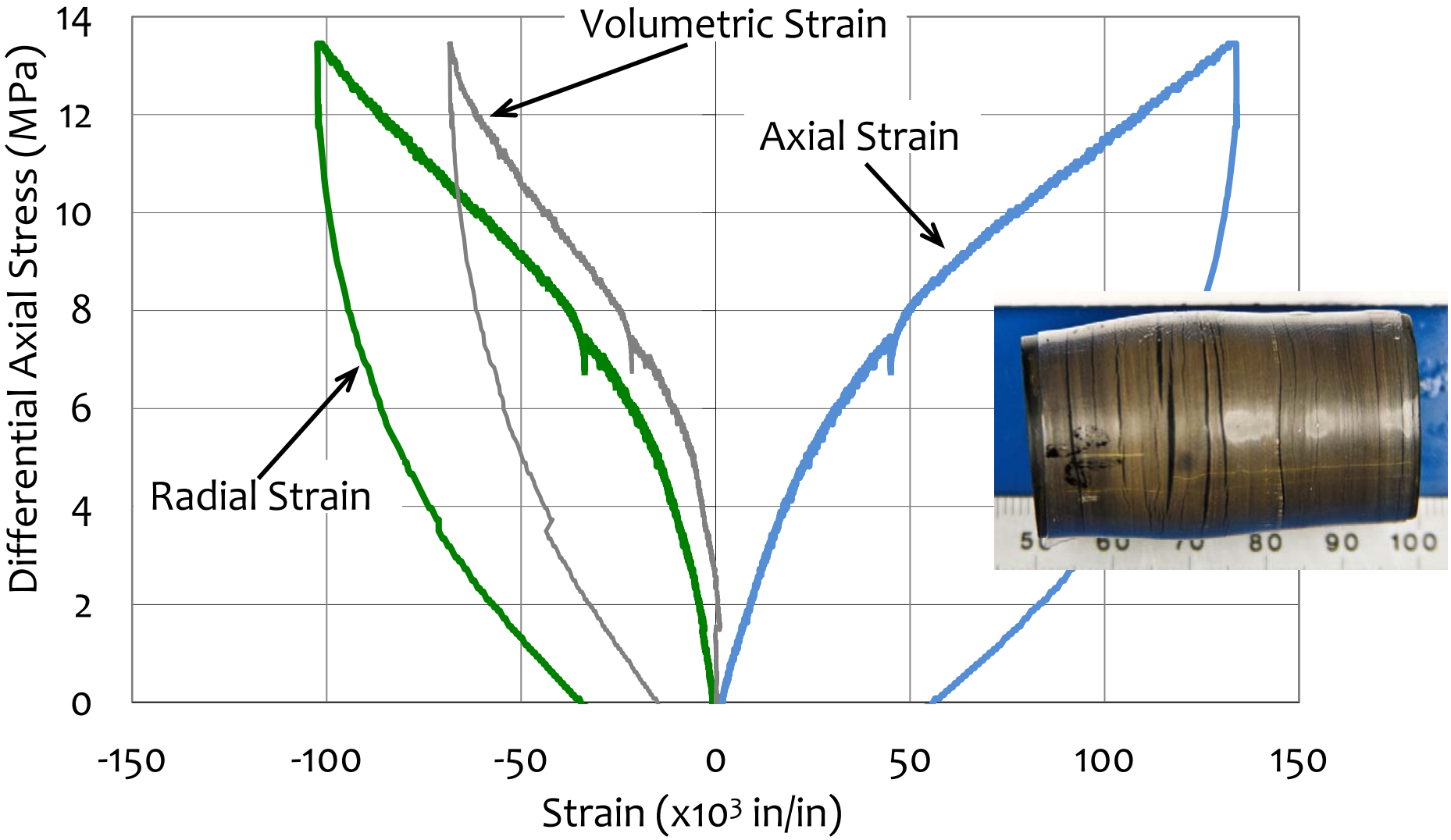

ICSE is exploring the most efficient way of incorporating these properties into models

- Hyperbolic relationships (Duncan-Chang) between stress and deformation
- Neural networking protocols to interrelate behavior to the governing independent variables (e.g., temperature, grade)

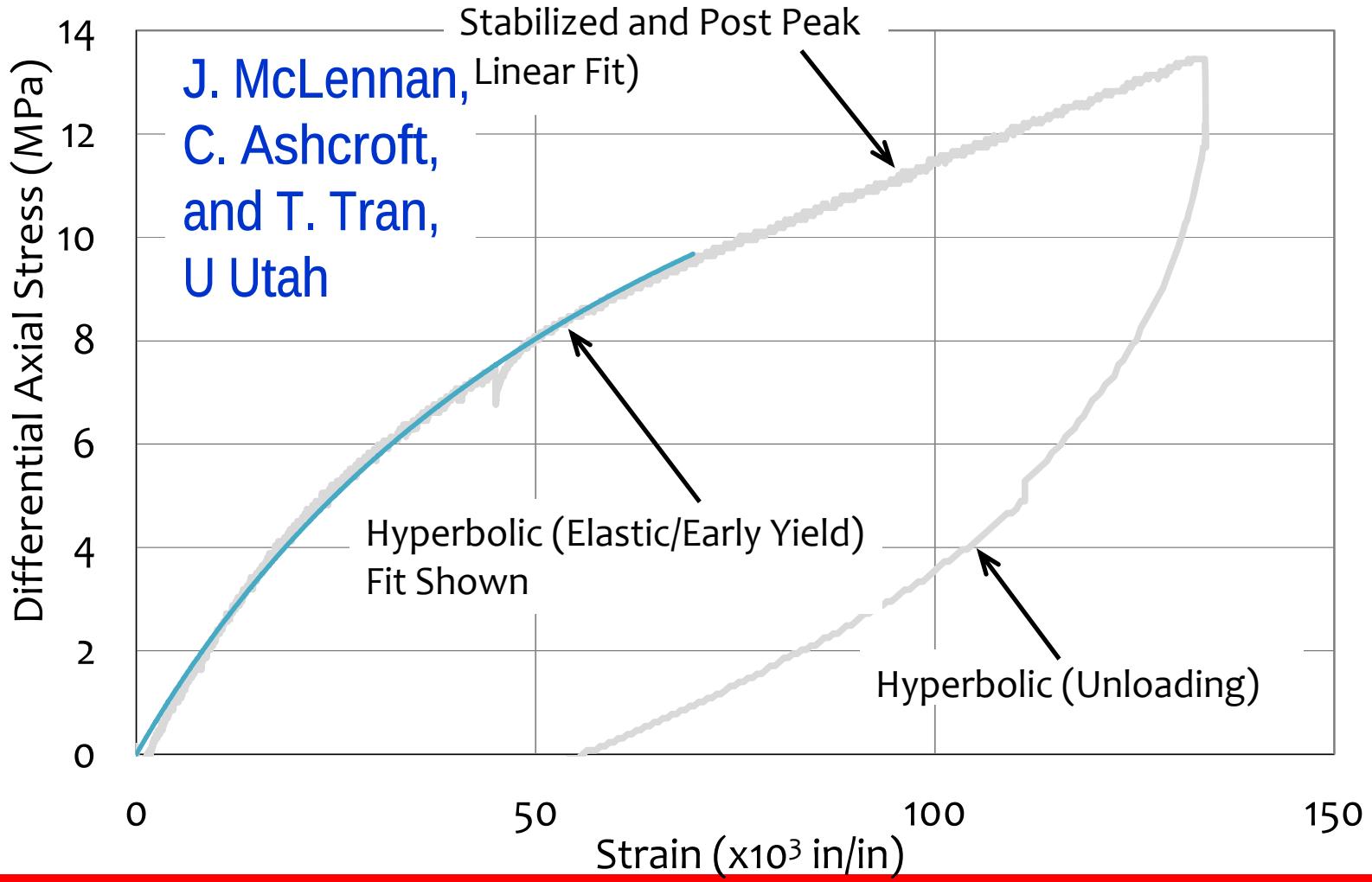

ICSE is calculating the relative importance of conduction and convection

Initial Computational Geometries

P. Smith, M. Hradisky, D. Coates, U Utah

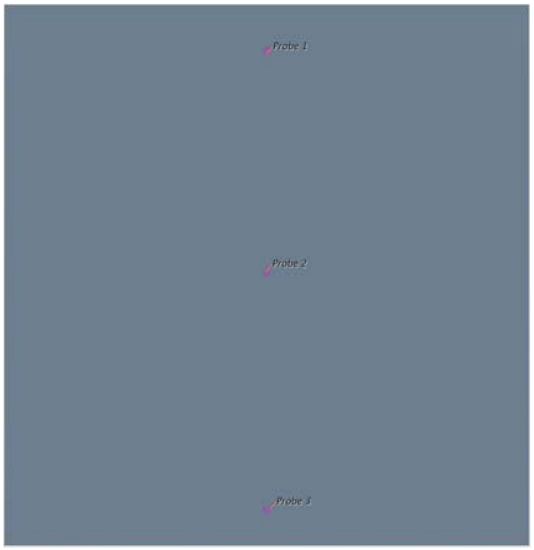

Solid shale

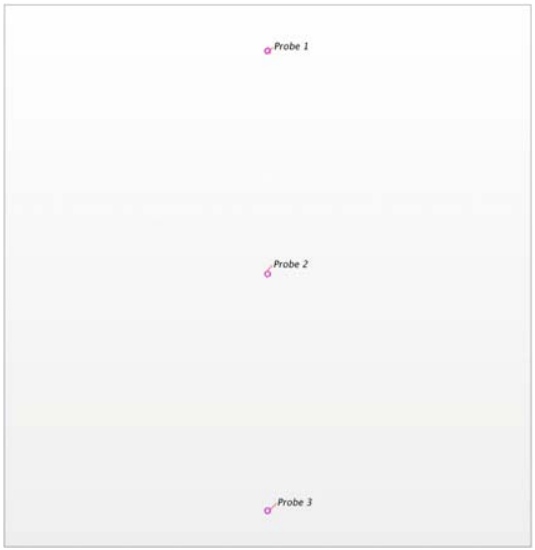

Empty volume

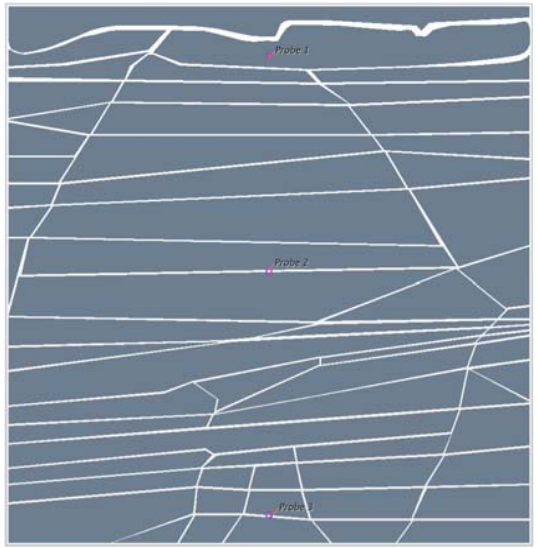

Crack size 0.005 m

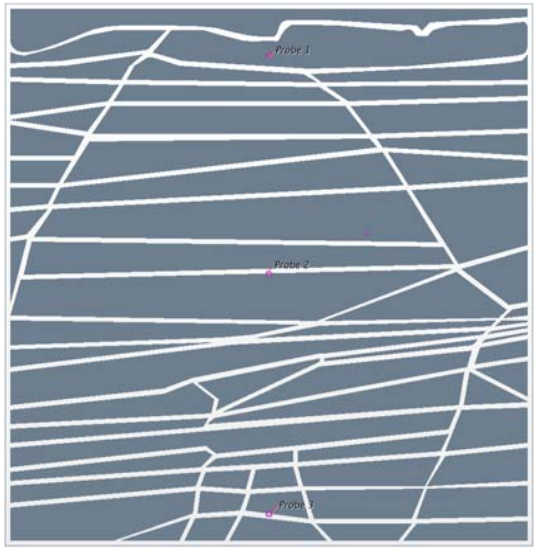

Crack size 0.010 m

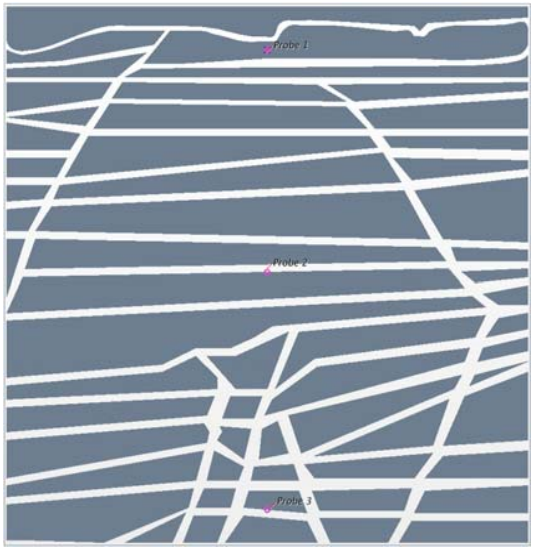

Crack size 0.015 m

Solid block heating with only thermal conduction

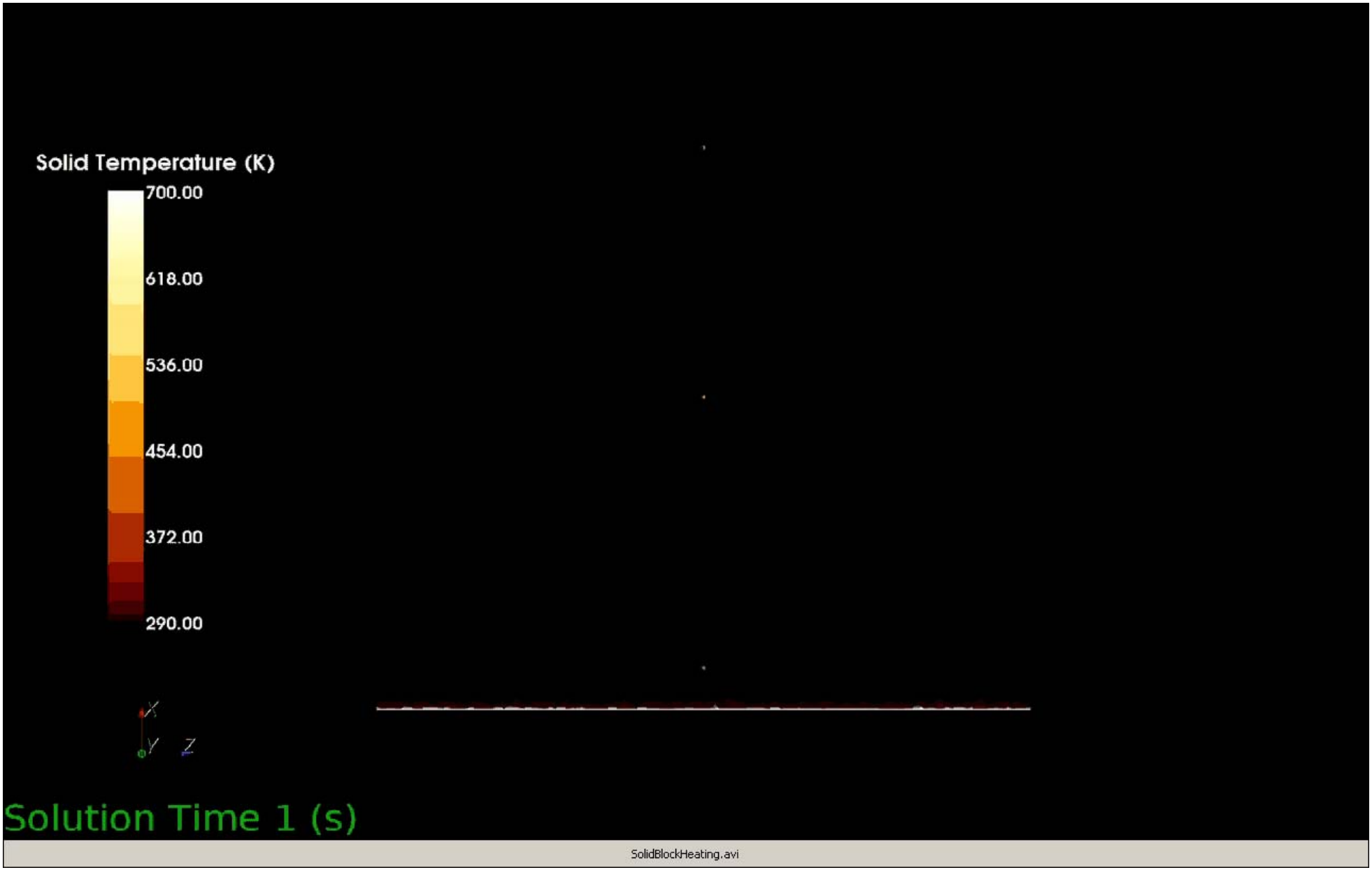

Convection in cracks alters the nature of the heat transfer

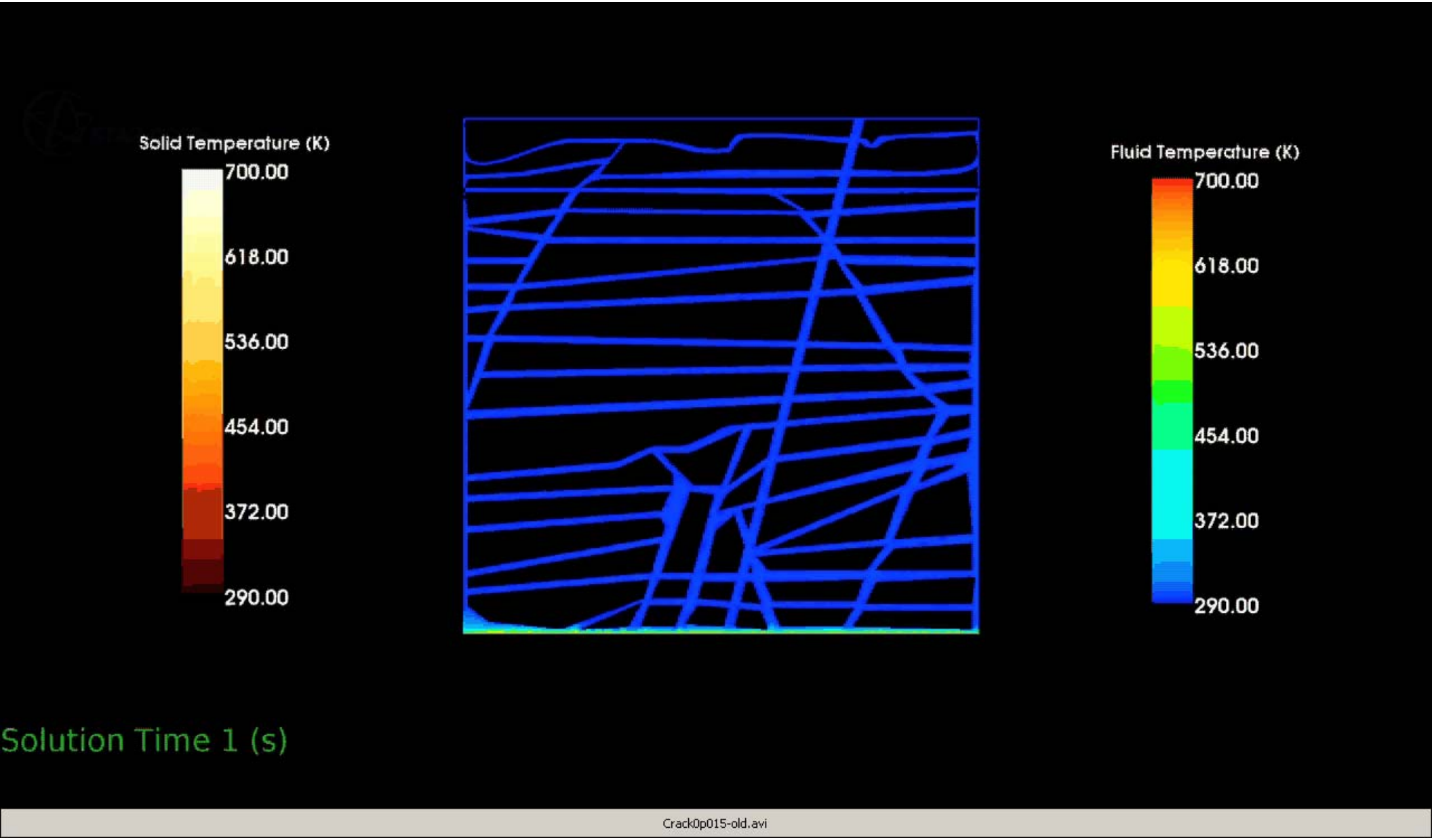

Our Pilot Test uses a triangular convection loop

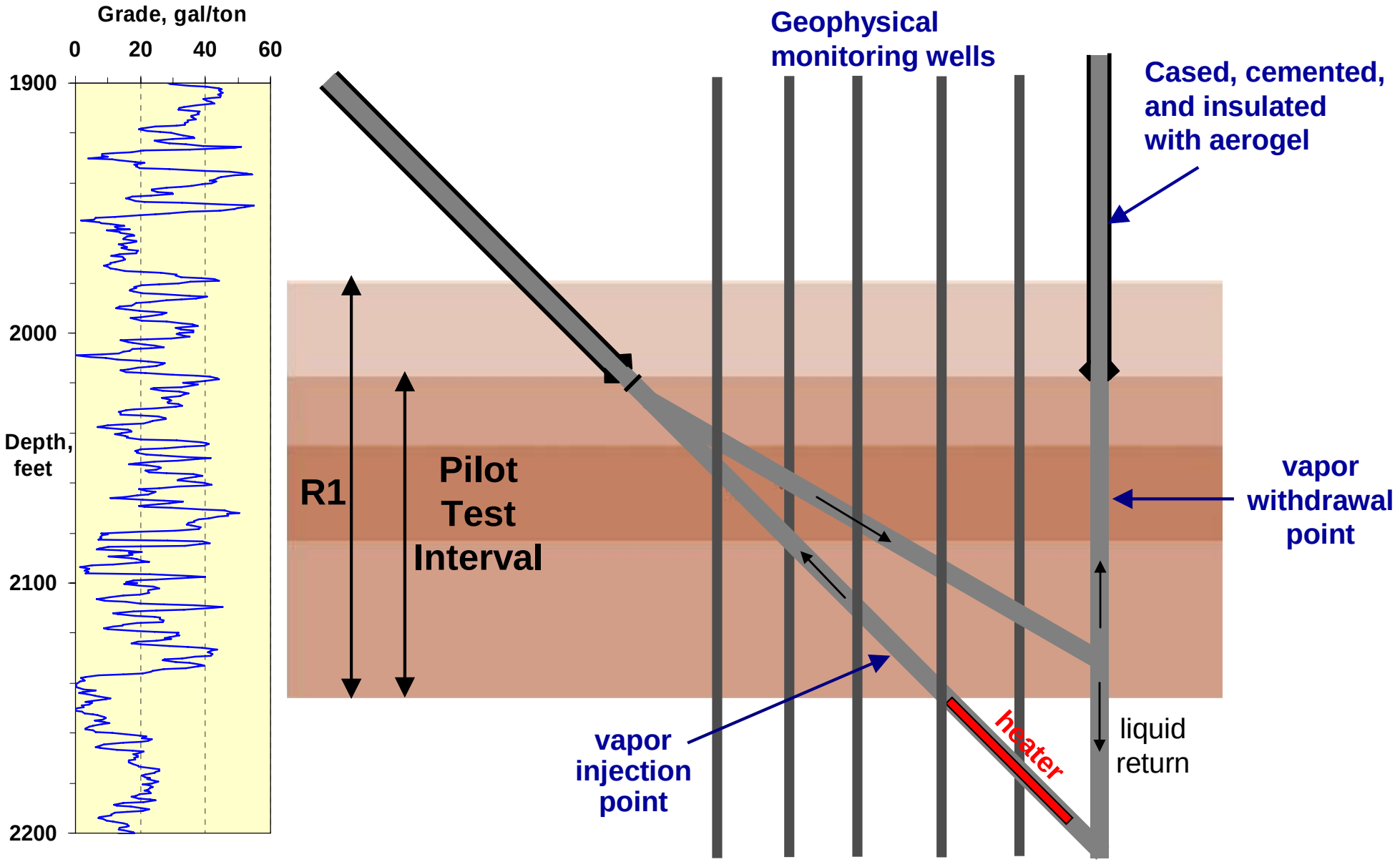

Our production well is insulated with silca aerogel, the best insulation known

Aerogel granules <1/8”

Carbon black added for blocking radiative heat transfer

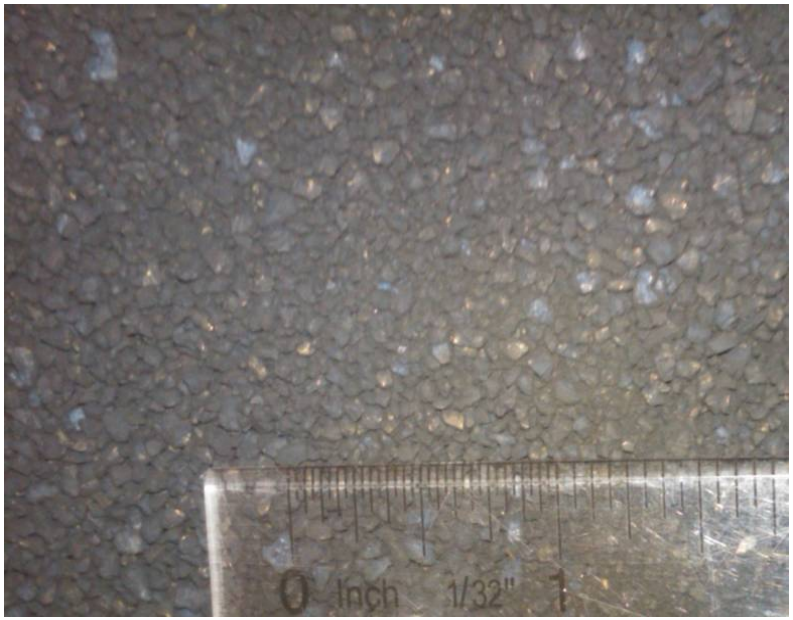

Filling the production well

We conducted a 3-day heater test in January to check out downhole equipment

- **Heater power up to about half its design value**
  - Limited by a leaky weld that prevented drawing a vacuum on the reflux heater
- **Discovered flaws in some other downhole equipment that required fixing**
- **The test propagated a steam front at about 250 ^{o}C up the lower lateral of the triangular convection loop.**
- **The heater test provided valuable information for benchmarking process models**

The heater test proved the excellent insulation value of aerogel

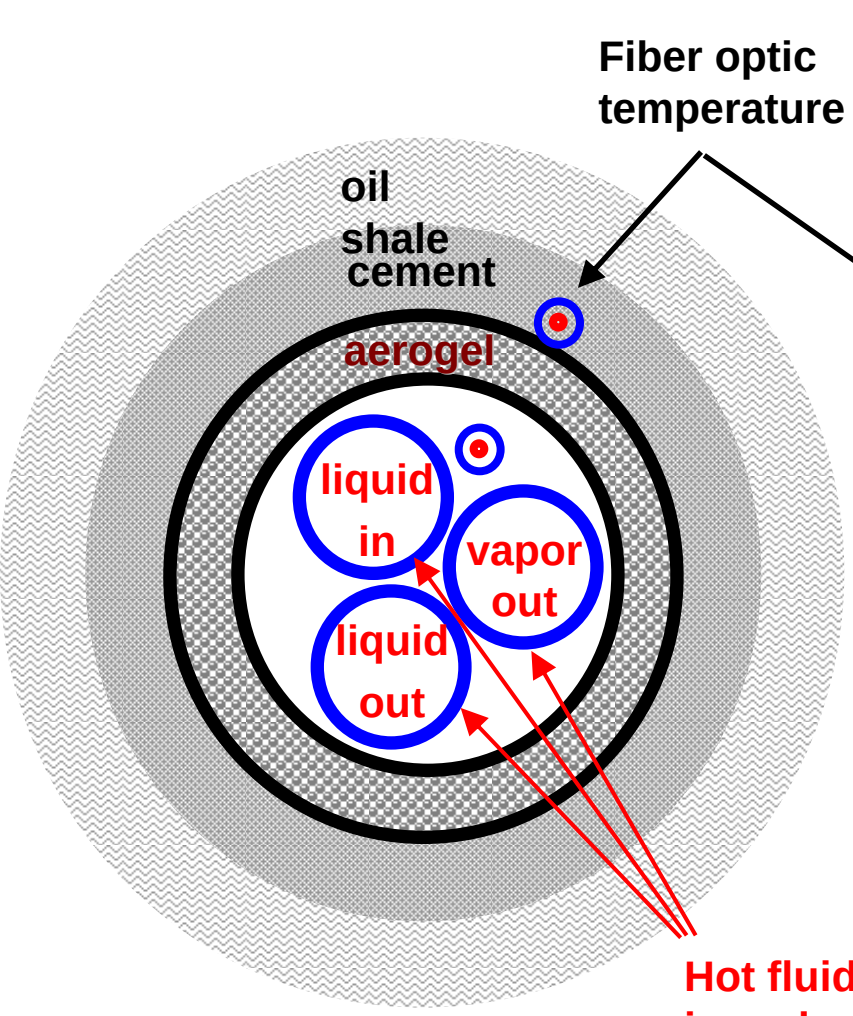

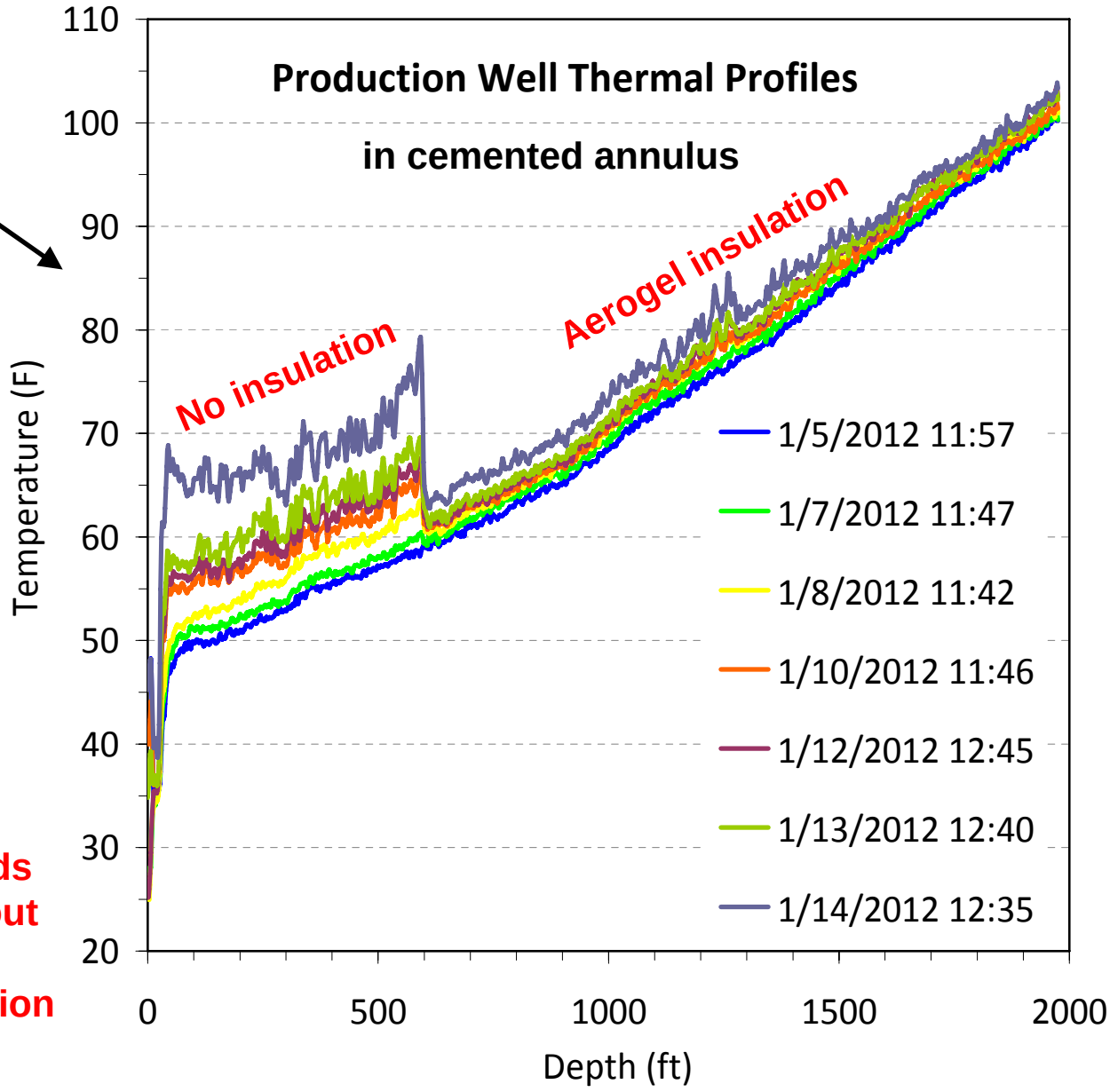

The Pilot Test has six geophysical monitoring wells, including fiber optic temperatures

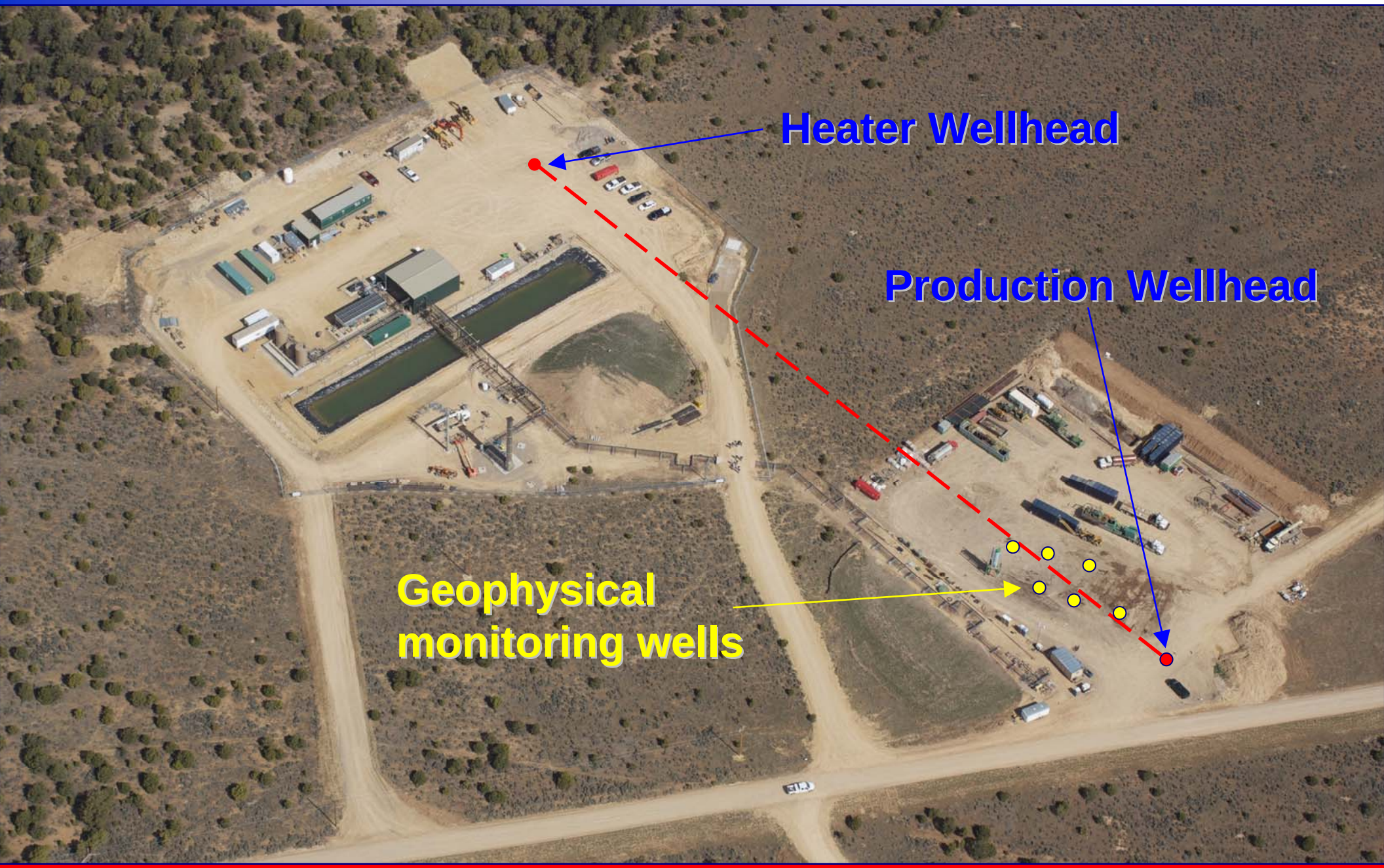

ICSE has constructed a 3D model of our Pilot Test well system for thermal simulation

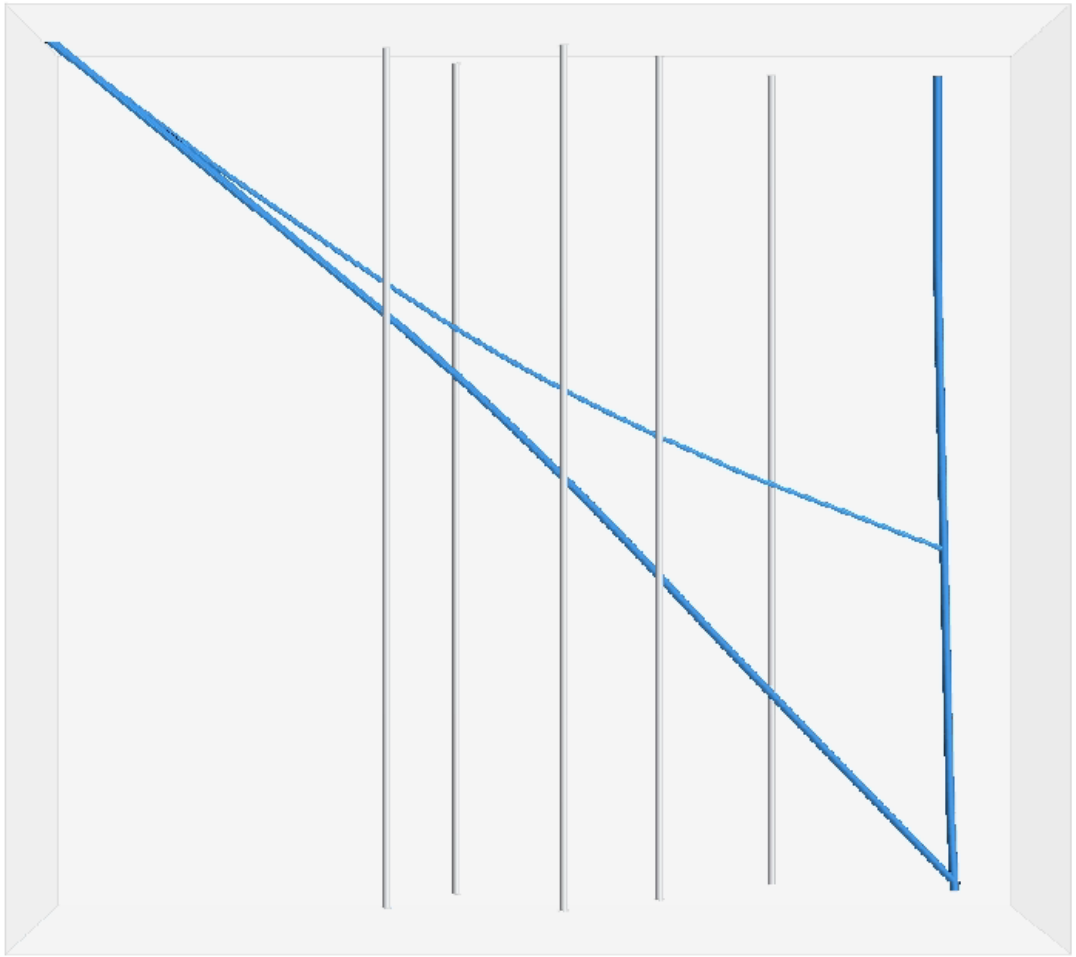

AMSO-HeaterTestGeometryOnly.avi

Temperature data from the TM wells will be used to calibrate thermal transport models

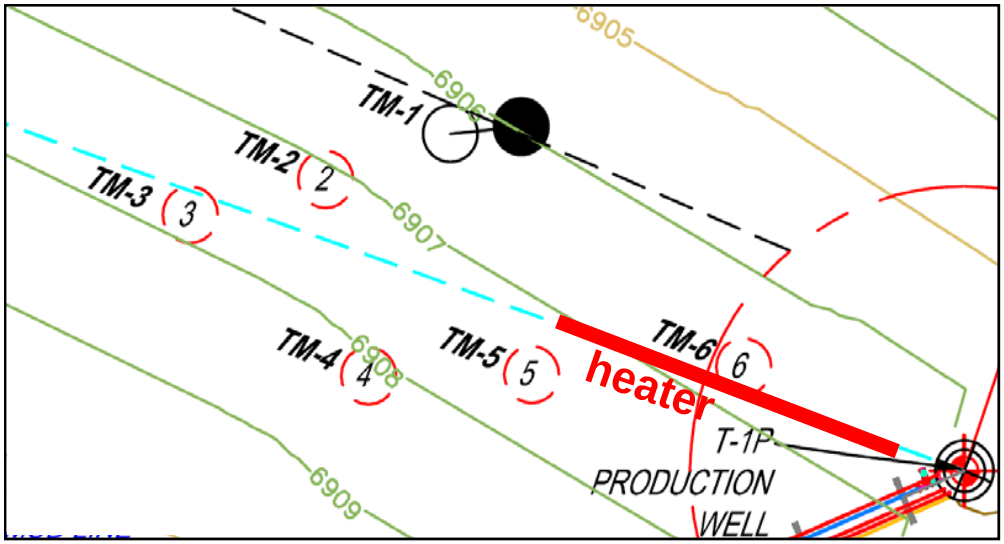

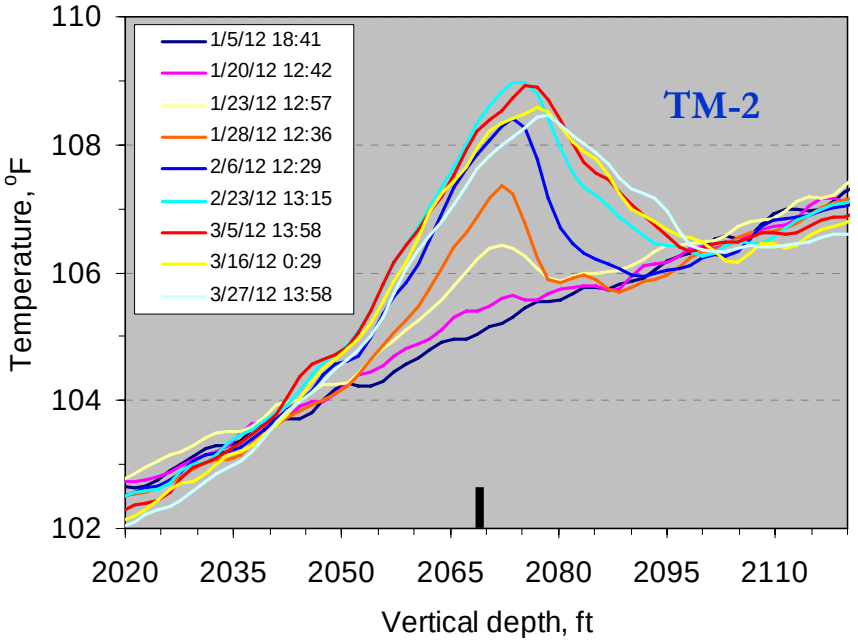

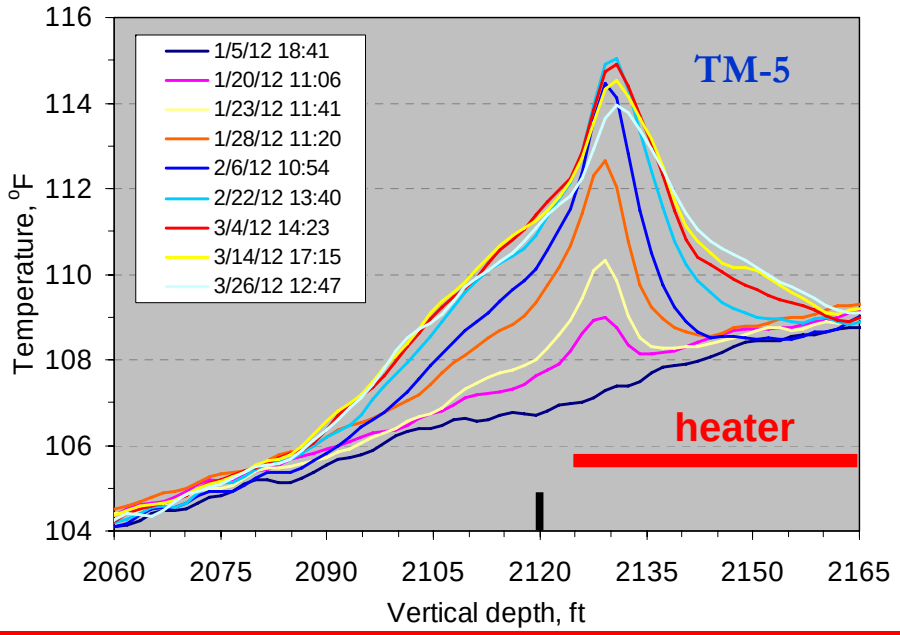

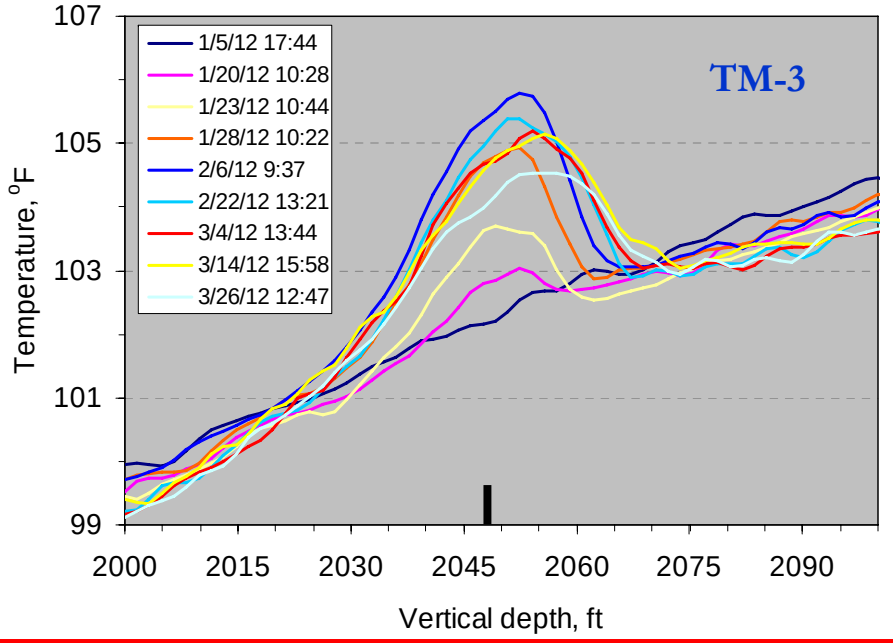

Time for temperature rise correlates with distance—ICSE is in the process of simulating

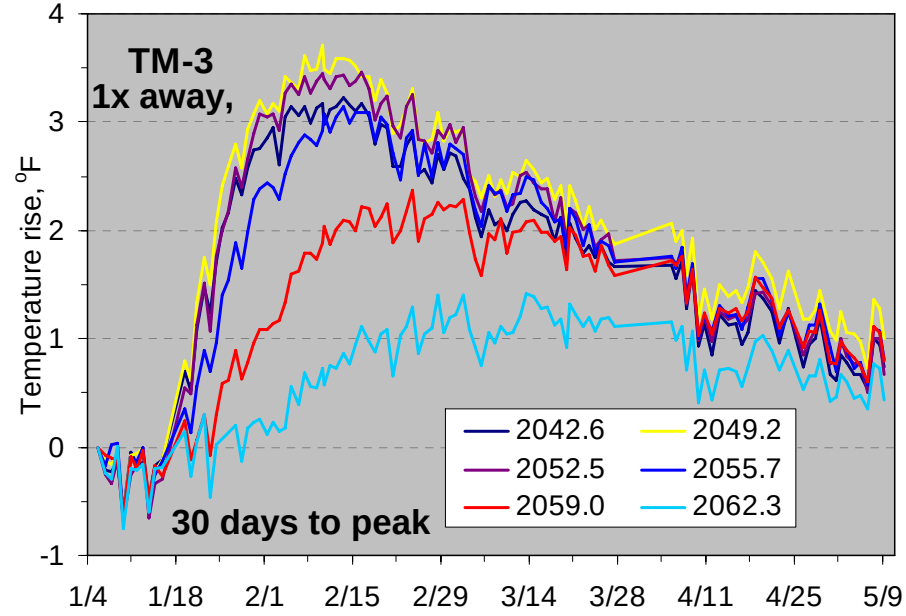

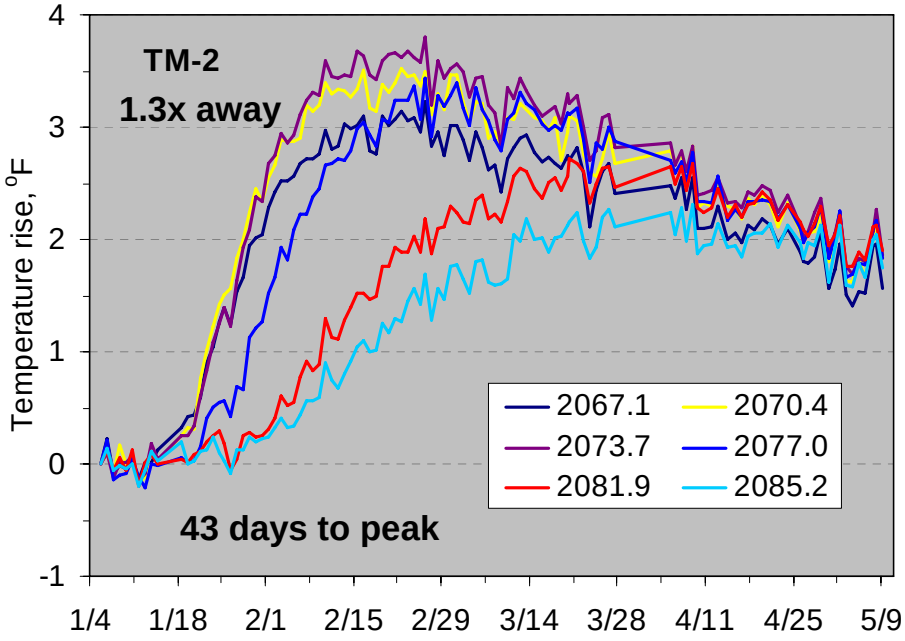

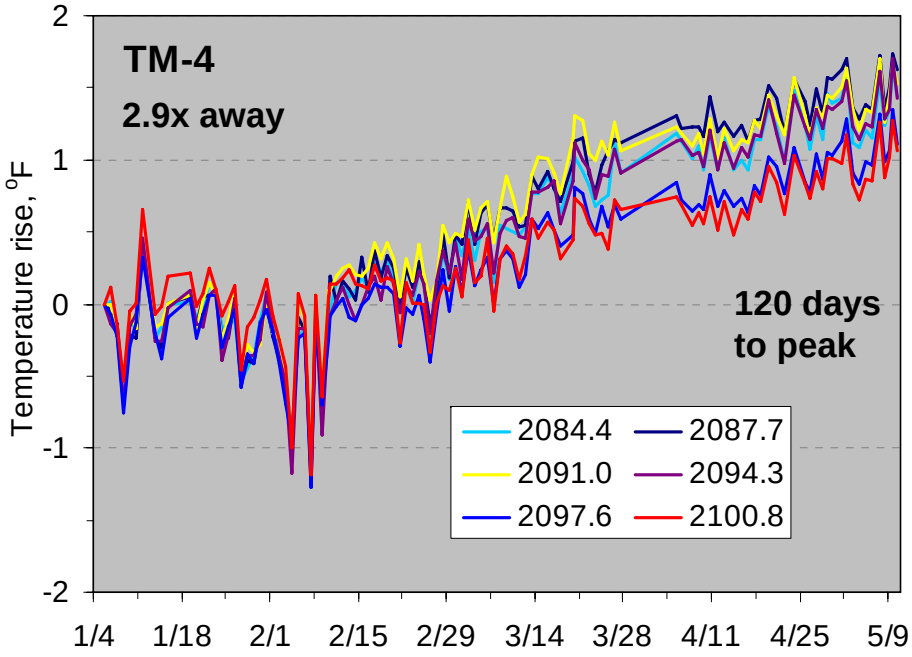

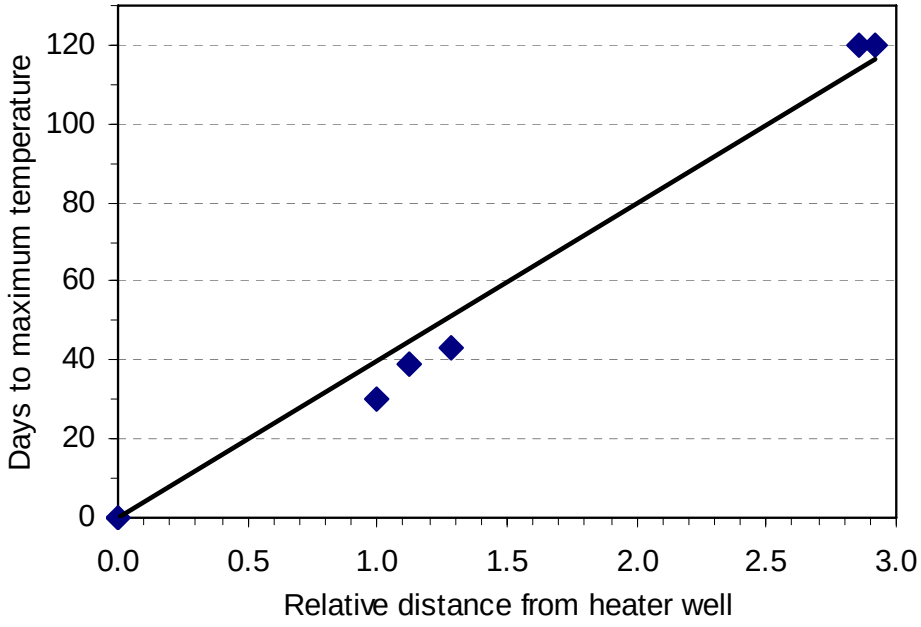

Pilot Status Summary

- Replacement parts were fabricated, and the heater casing and defective instrumentation have been reinstalled

- The heater is scheduled to arrive and be installed in late May
- Start of heating is estimated for late spring
- Completion of the pilot is estimated to be approximately the end of 2012